# A NUMERICAL AND EXPERIMENTAL INVESTIGATION OF A SUBSURFACE STEP USING FLASH THERMOGRAPHY

By

David Nejdl

## A THESIS

Submitted to
Michigan State University
in partial fulfillment of the requirements
for the degree of

Mechanical Engineering—Master of Science

2021

#### ABSTRACT

# A NUMERICAL AND EXPERIMENTAL INVESTIGATION OF A SUBSURFACE STEP USING FLASH THERMOGRAPHY

By

## David Nejdl

Flash thermography (FT) is a well-established non-destructive testing (NDT) technique that uses a short (~msec) pulse from a flashlamp to uniformly heat the surface of a sample and interrogate its subsurface structure based on the surface temperature response, measured with an infrared (IR) camera. Heat flow into a defect-free sample is described by a 1-D diffusion model, which transitions to higher dimensions due to subsurface discontinuities. 1-D approaches can be unreliable in the vicinity of abrupt thickness change, termed as the 'transition zone,' where lateral heat flow from the thin to thick region may mask surface temperature changes due to heat flowing into the part. In this work, we quantify the uncertainty in a "subsurface step," of a steel sample heated on its front flat and smooth surface, while the thickness (L) of the plate changes with a known step size (dL) on the backside. Finite element models simulating the FT process were developed to understand the effect of sub-surface steps on the thermal diffusion and compared with experiments for 12 varying step (dL/L) combinations. The width of the transition zone was measured using the Thermographic Signal Reconstruction (TSR) method. Results indicate that the transition zone can be defined simply as a function of its geometry. Experiments confirmed that the model predictions work well under the assumption that the steps are properly distinguishable from each other. Lastly, equations to estimate the detectability of a step were developed to be used in addition to the camera's detection limits. Overall, the approach used can be extended to anisotropic materials such as composites and bonded joints to enable efficient NDT of structural components.

#### **ACKNOWLEDGEMENTS**

Attending Michigan State University for graduate studies has been an extreme intellectual challenge to undertake, even more so when 75% of my time at the university has been during the global pandemic. I would like to extend my appreciation to the members of my committee; Dr. Mahmood Haq, Dr. Sara Roccabianca, and Dr. Gary Cloud for their time and effort spent reviewing my work.

I would like to thank my advisor, Dr. Mahmood Haq, for his support and encouragement to pursue higher education and for the unique opportunity in engaging in cutting edge research at a world-renowned research institution. His financial support and mentorship allowed me to work independently as a researcher, which was a rewarding challenge to undertake.

This work would not have been possible without the close collaboration of the team at Thermal Wave Imaging Inc. Specifically, I would like to thank Maria Beemer, Yulin Hou, Duy Tran, and finally Dr. Steven Shepard. I am extremely grateful to them as their expertise was crucial to my success. Additionally, I would like to extend my appreciation to the members of my research group, specifically to Erik Stitt, Fahad Hassan, and Evan Patton, all of whom have given guidance to be successful in graduate school. Finally, I would like to thank my family and my friends, whose support and encouragement gave me motivation to undertake this challenge.

This project was sponsored by the U.S. Air Force under Prime Contract No. FA8649-20-C-0015 which was issued to Thermal Wave Imaging, Inc. with Michigan State University as a Subcontractor. I would like to acknowledge the fellowship support from the department of Mechanical Engineering and the support from the faculty startup funds of Prof. Mahmood Haq in the department of Civil and Environmental Engineering.

# TABLE OF CONTENTS

LIST OF TABLES	V
LIST OF FIGURES	vi
Chapter 1: Introduction	
1.1 Flash Thermography and its Applications	
1.2 Mathematical Background	
1.3 Thermographic Signal Reconstruction	
Chapter 2: One Dimensional Modeling and Validation	8
2.1 Introduction	
2.2 Model Parameters	
2.3 Results and Discussion	
Chantan 2: Two Dimensional Modeline	22
Chapter 3: Two Dimensional Modeling	
3.1 Introduction	
3.2 Model Parameters	
3.3 Transition Zone Definition	
3.4 Results and Discussion	32
Chapter 4: Limits of Step Detectability	
4.1 Introduction	35
4.2 Detectability Equation	35
4.3 Results and Discussion	37
Chapter 5: Experimental Validation of Model Predictions	41
5.1 Introduction	
5.2 Steel Plate Design	41
5.3 Data Analysis	
5.4 Results and Discussion	
Chapter 6: Summary and Future Work	51
6.1 Summary	
6.2 Future Work	
6.2.1 Immediate Extension of Work	
6.2.2 Extension to Composites and Joints	
6.2.3 Alternative Data Processing Methods	
APPENDIX	57
WORKS CITED	60

# LIST OF TABLES

Table 2-1: Materials modeled and their thermal properties	10
Table 3-1: Design Geometry for varying step models	25
Table 3-2: Model parameters for transition zone width fit equation	33
Table 5-1: Machined geometry vs. designed geometry	43

# LIST OF FIGURES

Figure 1-1: a) A composite T-joint attached to a substrate b) a lap joint and c) a composite ramp structure
Figure 1-2: a) Subsurface steps in a T-joint, b) a subsurface step in a lap joint, c) subsurface steps in a composite ramp, and d) a single subsurface step, where the arrows indicate the incident heat pulse.
Figure 1-3: Natural logarithmic plot of the surface temperature vs time for an infinite and finite thickness stainless steel slab [7]
Figure 1-4: (a) Natural log plot for 4 mm thick stainless steel, its (b) first derivative, and (c) its second derivative, all which have been calculated with respect to ln(t) [7]
Figure 1-5: Raw and TSR logarithmic temperature for 2 and 5 ply thick sections in a composite [12]
Figure 2-1: Meshed geometry and boundary conditions, where the element size decreases when nearing the excited surface
Figure 2-2: Solution controls for second diffusion step in a composite material
Figure 2-3: Logarithmic temperature history for brass
Figure 2-4: 1st Derivative for brass
Figure 2-5: Second derivative for brass
Figure 2-6: Logarithmic temperature history for steel
Figure 2-7: First derivative for steel
Figure 2-8: Second derivative for steel
Figure 2-9: Logarithmic temperature history for an isotropic composite
Figure 2-10: First derivative for an isotropic composite
Figure 2-11: Second derivative for an isotropic composite
Figure 2-12: t* across all simulated slab thicknesses for brass
Figure 2-13: t* across all simulated slab thicknesses for steel
Figure 2-14: t* across all simulated slab thicknesses for an isotropic composite 21

Figure 2-15: Peak amplitude comparison for all three materials	22
Figure 3-1: Schematic of sample geometry (not to scale).	24
Figure 3-2: Mesh of a step geometry near the region of the step.	24
Figure 3-3: The second derivative on the thin side of a steel step (L=3 mm, dL=1 mm) at varying intervals	_
Figure 3-4: The second derivative on the thick side of a steel step (L=3 mm, dL=1 mm) at varying intervals	26
Figure 3-5: Variation in the peak second derivative amplitude across several geometries (L=3 mm) for brass.	28
Figure 3-6: Variation in the peak second derivative amplitude across several geometries (L=3 mm) for steel.	28
Figure 3-7: Variation in the peak second derivative amplitude across several geometries (L=3 mm) for an isotropic composite.	29
Figure 3-8: Contour plots of the second derivative with a varying step size	30
Figure 3-9: Curve fit to peak second derivative amplitude data for steel with L=3 mm and dL=1 mm.	
Figure 3-10: Sum of a negative and positive Gaussian pulse to form the curve fit of the peak second derivative amplitude data (L=3 mm, dL=1 mm).	31
Figure 3-11: Transition zone width regression model across all tested geometries and materials	
Figure 4-1: Temperature drop across a step for an isotropic carbon fiber material	38
Figure 4-2: Temperature drop across a step for a low carbon steel.	39
Figure 4-3: Temperature drop across a step for brass.	39
Figure 5-1: Modeled Geometry.	42
Figure 5-2: Machined Steel Plate	42
Figure 5-3: Schematic of parallel steps and series steps	43
Figure 5-4: Raw data in MATLAB in a) pixels and b) inches	44
Figure 5-5: a) Data taken from the series orientations and b) data taken across all parallel orientations.	45

Figure 5-6: Visualization of the extracted cross sections for series and parallel data	45
Figure 5-7: Sample curve fit for a single transition zone	46
Figure 5-8: Transition zone comparison across series (S) and parallel (P) normalized steps	47
Figure 5-9: a) Series and b) parallel temperature data at time t*	48
Figure 5-10: Sample temperature curve fit for a single step.	49
Figure 5-11: Temperature drop across all steps. A threshold for temperature drop in order to obtain a proper transition zone measurement was estimated to be at 90 mK	50
Figure 6-1: All properly measured transition zones.	52
Figure 6-2: Prediction of temperature drop across modified sample utilizing the same temperature threshold of 90 mK.	54

## Chapter 1: Introduction

## 1.1 Flash Thermography and its Applications

Flash thermography is an established nondestructive testing (NDT) technique which utilizes a short heat pulse from a flashlamp to heat the surface of a sample and investigate the subsurface structure by monitoring the surface temperature response as measured from an infrared (IR) camera. Flash thermography is an attractive choice for NDT as it is well suited for noncontact inspection while only requiring access to a single side of the part. Applications range widely, including detection of fatigue cracks in metals, detection of pores and voids, corrosion, delamination and damage in composite structures, damage in honeycomb composite panels, inspection in additive manufacturing, and even damage in panel paintings 0,[2],[3]. In comparison with other NDT methods, flash thermography is extremely fast, operating in seconds to minutes depending on material, and offers excellent defect visualization while remaining cost effective [4].

With an increased use of composite materials in aerospace, mechanical, and materials engineering, there is a need for a robust method for NDT for these materials. Early applications show its usefulness in identifying defects in aircraft repair and complex bonded structures [5],[6]. More recent contributions extend into automation to remove the dependence on a trained operator [2],[7],[8]. Oftentimes composite materials require adhesive bonding to form complex structures such as a T-joint or a lap joint as illustrated in Figure 1-1. Bonds can introduce defects in critical structural components and proper NDT of such structures is vital in ensuring safe operating conditions.



Figure 1-1: a) A composite T-joint attached to a substrate b) a lap joint and c) a composite ramp structure.

Even, for example, if the structures shown in Figure 1-1 were made of a single flawless piece of metal, there would be challenges associated with using flash thermography to investigate their structure. A sudden subsurface geometry change will cause an area of two-dimensional heat flow to occur, disturbing the heat signal as recorded by the IR camera. The objective for this work is to investigate the purely geometrical effect of a subsurface step in the processing of one-dimensional flash thermography data. In all cases of Figure 1-1, there exists a subsurface step if the incident heat pulse is received from the bottom of the structure as highlighted in Figure 1-2. This work will be simplified by utilizing a structure similar to Figure 1-2d.

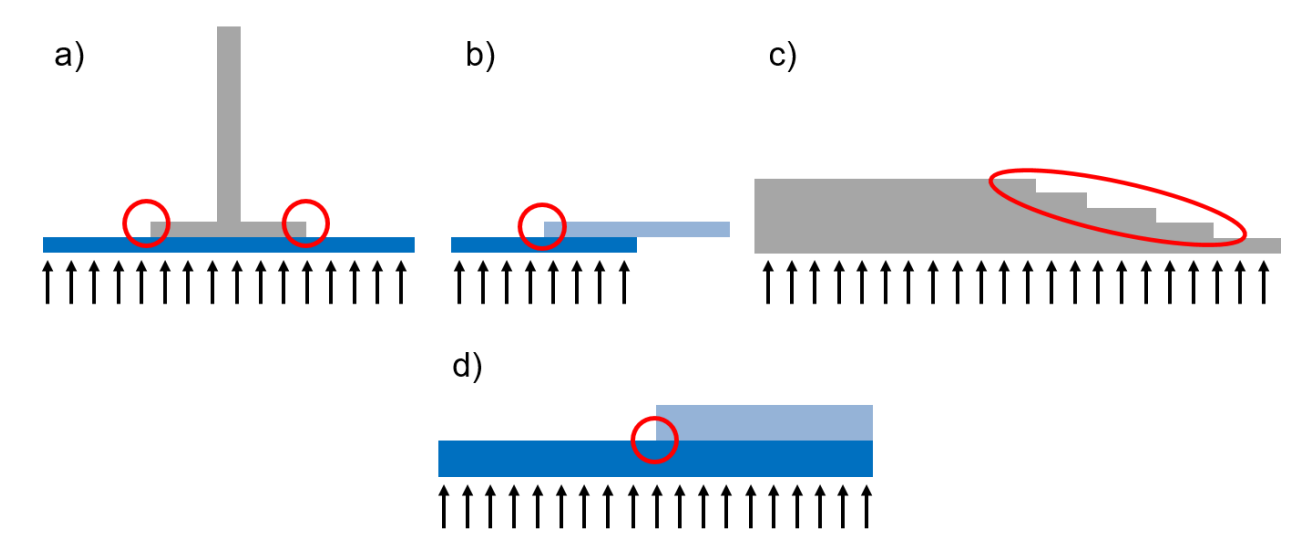


Figure 1-2: a) Subsurface steps in a T-joint, b) a subsurface step in a lap joint, c) subsurface steps in a composite ramp, and d) a single subsurface step, where the arrows indicate the incident heat pulse.

#### 1.2 Mathematical Background

Analytical solutions that are capable of fully describing an ideal flash thermography setup are well known and available in typical heat transfer reference texts [9]. Under a typical single pixel approach, the simplest case to solve is a defect free, one dimensional infinite slab that is heated by an instantaneous heat source. The surface temperature for such a scenario is given by

$$\Delta T(t) = \frac{Q}{e\sqrt{\pi t}}$$
 1.1

where Q is the energy flux absorbed, and e is the thermal effusivity, defined as

$$e = \sqrt{k\rho C}$$

where k,  $\rho$ , and C are the thermal conductivity, density, and the heat capacity respectively.

This solution is primarily useful when taking the natural logarithm, where the solution then becomes

$$\ln(\Delta T) = \ln\frac{Q}{e} - 0.5\ln(\pi t)$$

If Equation 1.3 is plotted, the logarithmic surface temperature becomes a straight line that is dependent on the natural log of time, with an exact slope of -0.5.

This result translates well to the more realistic scenario of a finite slab with thickness L.

The natural log behavior of the finite slab is identical to that of the infinite slab except that it deviates from the straight-line behavior at time t\*, where the slope begins to level off to zero.

Plots for the infinite thickness and the finite thickness slabs are illustrated in Figure 1-3 below.

The surface temperature for the finite thickness case can be described analytically by

$$\Delta T(t) = \frac{Q}{\rho CL} \left[ 1 + 2 \sum_{n=1}^{\infty} e^{-\frac{\alpha n^2 \pi^2 t}{L^2}} \right]$$
 1.4

where  $\alpha$  is the thermal diffusivity, and L is the thickness. Finally t\* [10], [11] is given by

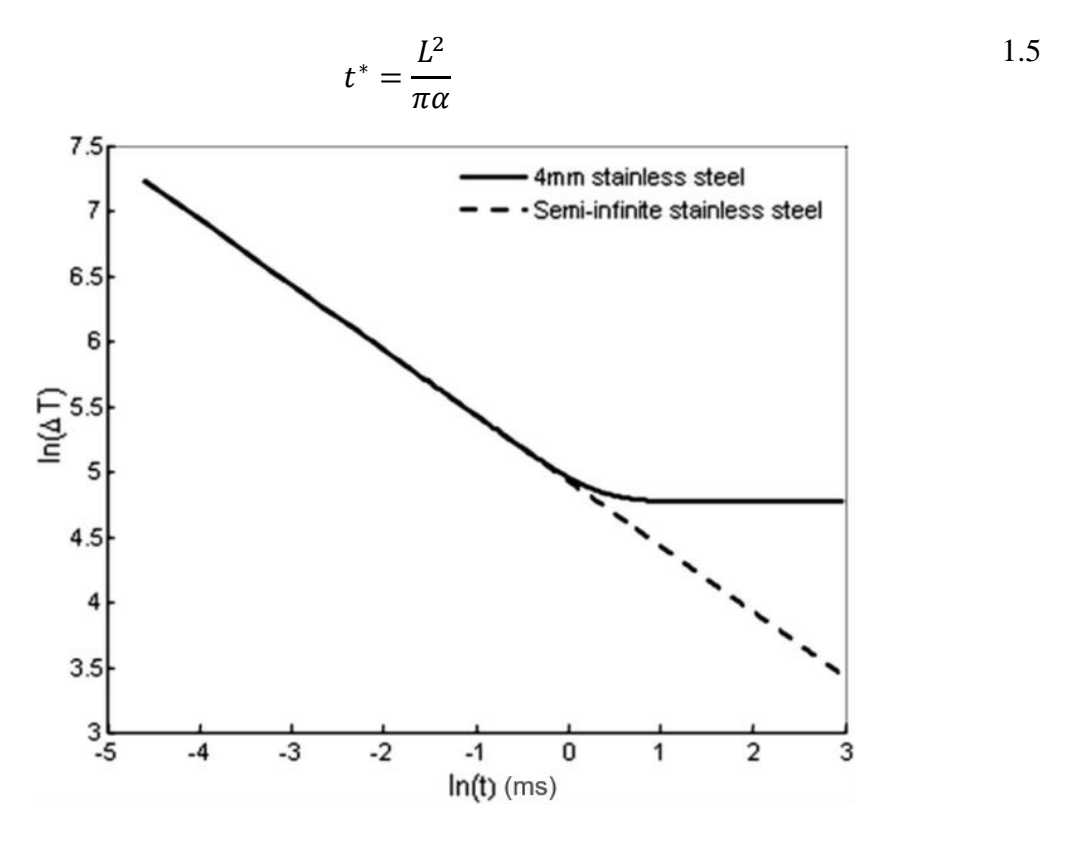


Figure 1-3: Natural logarithmic plot of the surface temperature vs time for an infinite and finite thickness stainless steel slab [7].

The first derivative of the natural logarithm of Equation 1.4 with respect to  $\ln(t)$  results in straight line behavior at -0.5, a transition region, and another straight-line behavior at 0. Now, differentiation of the first derivative, again with respect to  $\ln(t)$ , results in the  $2^{\rm nd}$  derivative being 0 at all times, other than the transition between the periods of a dominant 1D diffusion, and when 1D diffusion stops. The log plot, corresponding first derivative, and corresponding second derivative can be seen below in Figure 1-4.

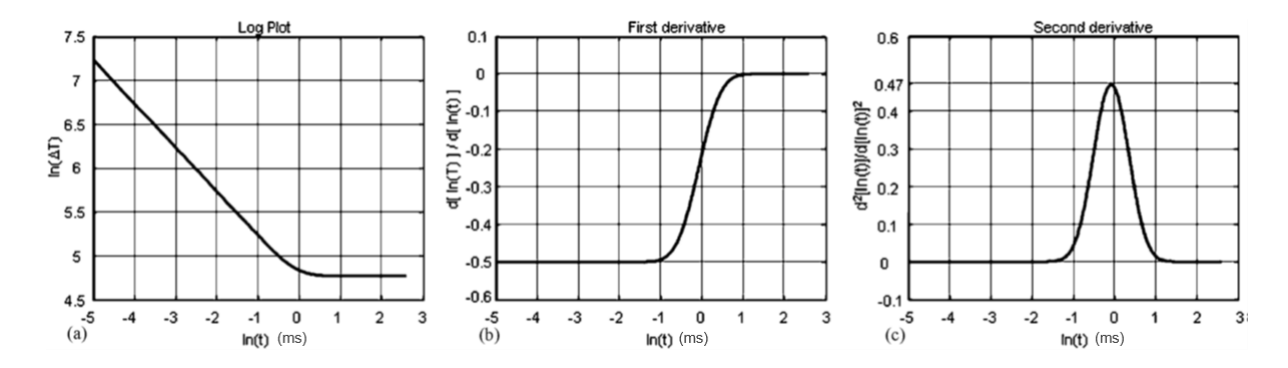


Figure 1-4: (a) Natural log plot for 4 mm thick stainless steel, its (b) first derivative, and (c) its second derivative, all which have been calculated with respect to ln(t) [7].

Shepard [7] has conveniently outlined the importance of several characteristics of the logarithmic second derivative. The second derivative is extremely useful in interpretation of NDT data because it highlights the deviation from ideal diffusion. In the infinite slab, the second derivative would always be zero. However, in the finite slab, there is a Gaussian peak due to the presence of the adiabatic back wall. The region prior to the pulse represents the early diffusion and the region after the peak describes transfer of heat away from the back wall, whether it would be convection, radiation, etc.

The logarithmic second derivative has several properties that allow it to be easily used in analyzing NDT data. Taking the second derivative of the natural logarithm of Equation 1.4 with respect to  $\ln(t)$  removes the dependence on the heat flux, Q, and thus makes it invariant to the energy amplitude. Additionally, in the adiabatic case, the size and shape of the second derivative will be invariant to the material, and will only shift the time at which the peak occurs based on the thickness or material composition of the slab. This Gaussian pulse can be confidently described with a peak amplitude at 0.47. Coupling this fact along with the known  $t^*$  occurring at the time of the peak amplitude of the logarithmic second derivative, we have two very powerful characteristics to compare NDT data to. Shepard [7] has also shown that the second derivative

acquired experimentally showed that the peak amplitude was in good agreement with the analytical logarithmic second derivative peak of 0.47. He concluded that the difference in peaks could be attributed to the fact that the experimental setup cannot be adiabatically isolated.

### 1.3 Thermographic Signal Reconstruction

Experimental analysis of flash thermography data relies on Thermographic Signal Reconstruction (TSR). For flash thermography, the aspect ratio of any defect is defined as its diameter to depth ratio. As this ratio reduces to less than or equal to one, the temperature difference between the defect and the surrounding areas decreases such that it is comparable to the noise level of the IR camera [12]. For measurement of defects like this or for measuring physical properties of material, additional signal processing is required and this is where TSR finds its place.

The TSR process fits a low order polynomial to the logarithmic time history for each pixel, resulting in a reduced noise signal as seen in Figure 1-5 [12]. By representing TSR data in a closed form, it can be easily manipulated to obtain subsequent derivatives without introducing additional noise. In section 1.2, derivatives were shown to highlight the difference between undisturbed diffusion and a subsurface defect or geometry change. By applying the TSR technique to experimental data, we can easily extract information about the depth of a sample or depth of a flaw given that the material's diffusivity is known. We can also determine the sample diffusivity given the depth of the sample or flaw depth. In comparison to other data processing methods, TSR often gives excellent performance with respect to the signal-to-noise ratio, experimental reliability, and prediction of depth and material [13]. With respect to composite materials, TSR has been shown to contribute a reduction of the temporal noise, improve visual

detection, and make a significant contribution to the ease of detecting defects in flash thermography [14].

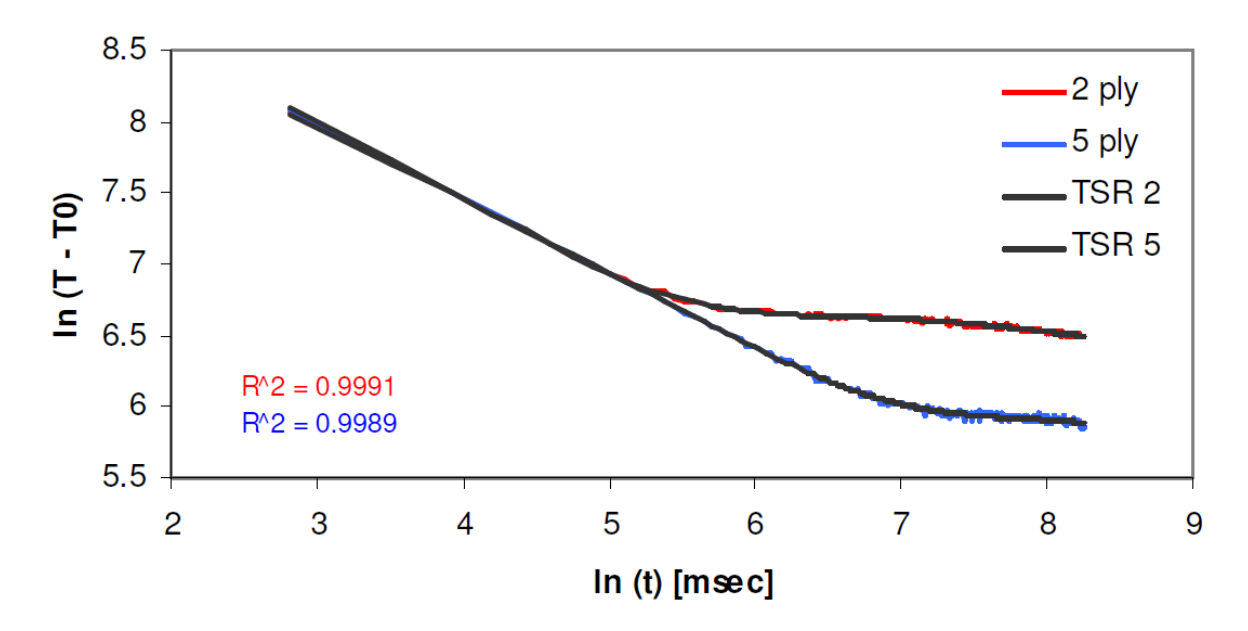


Figure 1-5: Raw and TSR logarithmic temperature for 2 and 5 ply thick sections in a composite [12].

# Chapter 2: One Dimensional Modeling and Validation

#### 2.1 Introduction

With any numerical analysis, it is oftentimes useful to solve a known problem to ensure a working analysis before advancing on to a more complex model. For this, we choose to simply solve the problem of a finite thickness slab with adiabatic boundary conditions, subjected to an instantaneous heat flux. This can be described mathematically as:

$$\frac{\partial T}{\partial t} = \alpha \frac{\partial^2 T}{\partial x^2}$$
 2.1

$$0 \le x \le L, \qquad t > 0 \tag{2.2}$$

with boundary and initial conditions

$$\frac{\partial T}{\partial x} = 0$$

$$x = 0, \qquad x = L, \qquad t \ge 0$$
 2.4

$$-k\frac{\partial T}{\partial t} = Q\delta(t)$$
 2.5

$$x = 0, t = 0$$
 2.6

$$T(x,0) = T_0 2.7$$

The partial differential equation and boundary / initial conditions described by Equation 2.1 through Equation 2.7 provides the analytical solution that was previously described in Equation 1.4. The finite element package ABAQUS® was chosen to solve numerically the problem described above. It is also worth noting that within finite element modeling, an instantaneous

boundary condition cannot be applied. Therefore, for this boundary condition, we applied a large heat flux for 1 ms.

Since a typical flash thermography experiment relies heavily on the 2<sup>nd</sup> derivative, namely t\* and its corresponding amplitude, we used the model t\* and corresponding amplitude to calibrate and fine tune the finite element model.

#### 2.2 Model Parameters

A two-dimensional model was generated within the ABAQUS® graphical user interface (GUI) with a width of 40 mm and a varying thickness, L. The base thickness, L, was chosen to be 3.0 mm, 3.1 mm, 3.2 mm, 3.5 mm, and 4.0 mm in order to obtain t\* and amplitude values across a range of thicknesses, and the results were compared to known, theoretical values. The initial temperature was prescribed to be ambient room temperature, and a 1 ms surface flux of 25 kJ/m² was applied. This heat flux was chosen as it has been estimated to be the maximum possible heat flux from a typical experimental flash thermography system [15]. In finite element modeling of heat transfer, applying no boundary conditions on a surface imposes a zero flux condition on that surface. Therefore, no boundary conditions were applied to the back or side walls, as this would force adiabatic boundary conditions on these surfaces. Following the excitation phase, a subsequent cooling phase was defined in order to allow heat to diffuse through the material completely. This cooling phase(s) varies based on the material selected, as the rates of heat-diffusion is material dependent, and is described in the following paragraphs.

Modeling was initially done for a composite material with isotropic heat conduction properties, but steel and brass were added to save computation time due to the long diffusion process involved with composites and also to make the study more robust by investigating

multiple materials which exist on different diffusive time scales. These materials and their properties are included in Table 2-1.

Table 2-1: Materials modeled and their thermal properties

Material	Conductivity	Density	Specific Heat	Diffusivity
Composite	0.8 W/mK	$1.6 \text{ g/cm}^3$	1.2 J/gC	$4.17E-7 \text{ m}^2/\text{s}$
Steel	49.6 W/mK	$7.6 \text{ g/cm}^3$	0.473 J/gC	$1.38E-5 \text{ m}^2/\text{s}$
Brass	124 W/mK	$8.49 \text{ g/cm}^3$	0.380 J/gC	$3.84E-5 \text{ m}^2/\text{s}$

Initially, the model was meshed with DC2D4 linear 2D heat transfer elements with an element size of 0.2 mm and time increment of 5 ms for both the initial excitation phase of 5 ms and the subsequent diffusion of the heat through the body. However, not only did this setup not provide proper spatial resolution as there was poor element resolution near the excited surface, but it also gave poor time resolution as it became difficult to accurately determine the peak time (t\*) and its corresponding amplitude from the second derivative. Subsequently, the mesh along the width was prescribed such that the elements would be 1 mm in width but a mesh bias was introduced towards the excited surface so that the element size would decrease and become thinner as the elements got closer to the excited surface. The time was adjusted such that the excitation phase lasted 1 ms and had a time increment of 0.1 ms. A schematic of the mesh and boundaries is shown in Figure 2-1.

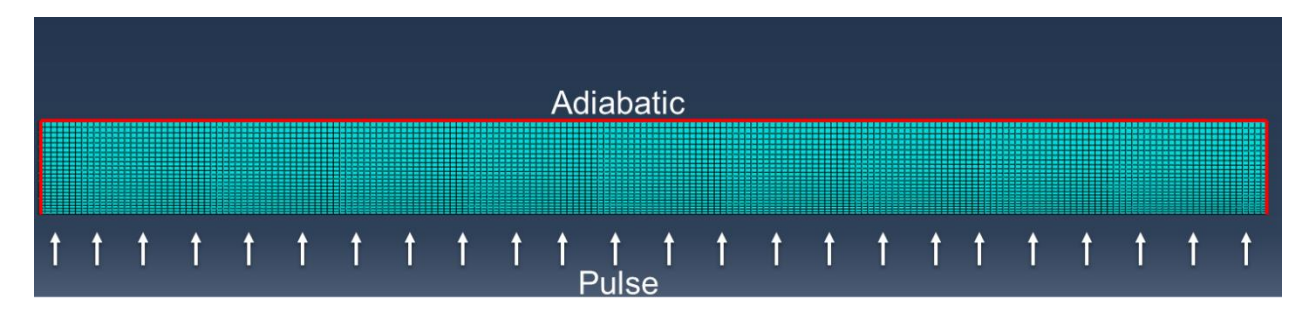


Figure 2-1: Meshed geometry and boundary conditions, where the element size decreases when nearing the excited surface.

For the subsequent cooling and diffusion phase, it is important to balance the computation time with the time required for complete diffusion of heat through the material. For this, metals (steel and brass) have a single cooling phase where the time increments by a constant 1 ms for 20s and 5s (respectively), which allows for complete heat diffusion. To reduce storage resources from incrementing every 1 ms, data was instead written every 5 ms to achieve balance of accurate computation and reduced storage space. However, the composite material has slower diffusivity by two orders of magnitude and using this same time increments would not only cause the simulation to run for days, but also take up an immense amount of storage. To combat this problem, two cooling phases were defined. The first uses a constant time increment of 1 ms that allows the heat to diffuse just enough so that we can confidently extract enough information such that the Gaussian pulse from the second derivative can be clearly defined. The second cooling phase implements an evolving time increment such that the time steps increase from 1 ms to 0.25s over a range of 285 seconds to complete the diffusion. This was done by setting an initial time step and a maximum time step within the step settings. In order to modify the increments such that ABAQUS® doesn't immediately choose the maximum step size, the general solution controls were modified such that the next time step could only be 1.001 times the previous step as highlighted in Figure 2-2. This measure also ensures that we get smooth data over time. This second cooling phase essentially allows us to confirm that the second derivative reaches and stays at its final value of 0 while allowing us to have a completed Gaussian pulse. This step was also essential in recognizing two dimensional heat flow in long diffusive processes in composites.

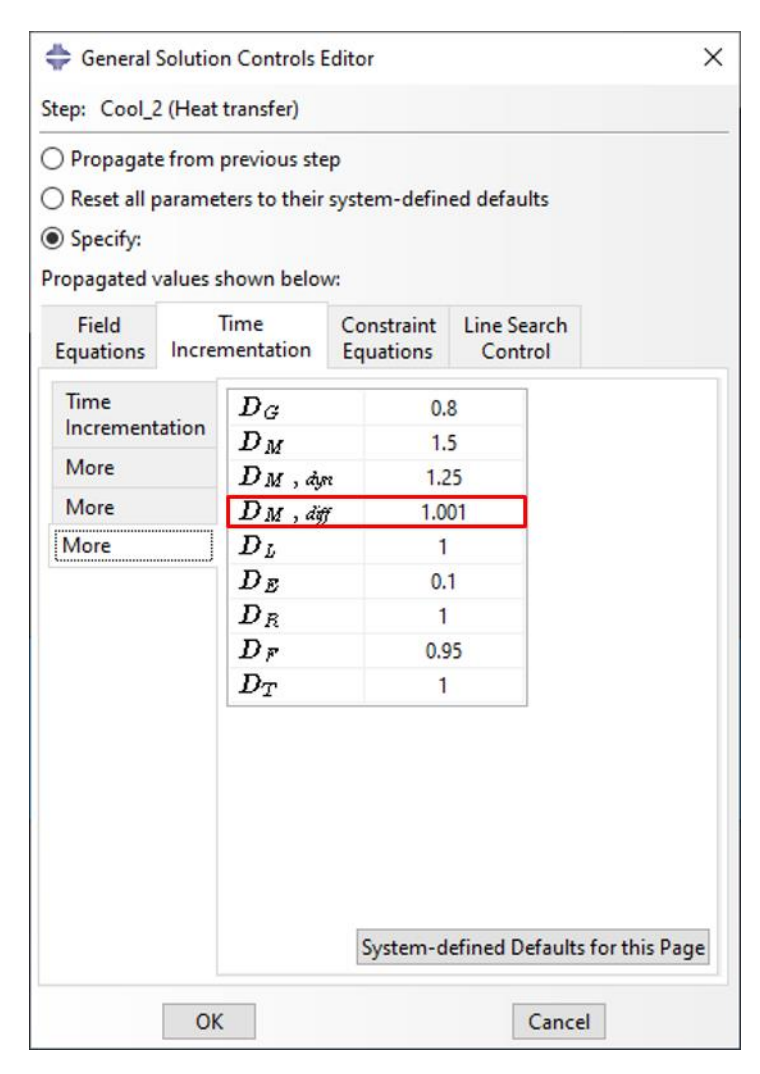


Figure 2-2: Solution controls for second diffusion step in a composite material.

#### 2.3 Results and Discussion

Nodal temperature data was extracted for all nodes along the excited surface and exported into MATLAB. Within MATLAB, the nodal temperature data was shifted in time by the length of the heat pulse (1 ms) such that the peak temperature would occur at time equal to 0, effectively becoming an instantaneous heat pulse. Next, the natural logarithm of both the time and the change in temperature  $(T - T_0)$  were obtained.

The next step was to take the first and second derivative of the natural log of the change in temperature. By taking the data to the natural log domain, we create an array such that we have

unequal spacing between points in time, making standard numerical derivatives ineffective at producing smooth derivatives of the numerical data. In order to take proper derivatives, a sliding and growing window scheme was provided to take numerical derivatives in the natural log domain. This function (see Appendix A) is defined as

NumericDerivative(x,y,InitPoints,GrowStart) and works by taking inputs of the x and y data  $(\ln(t))$  and  $\ln(T-T_0)$  respectively), the starting number of points for which to begin differentiation (for example starting with a derivative across 5 points) which also functions as the starting window size, and a point to begin the expanding window (for example – set to 0.50 to start expanding at 50% of the data). This function was used in an iterative process where the 3<sup>rd</sup> and 4<sup>th</sup> inputs were adjusted until the first derivative was smooth and noise-free and resembled an error function as seen in Figure 1-4b. This iterative process was again repeated to obtain a second derivative which was smooth and resembled a Gaussian pulse as seen in Figure 1-4c. From the second derivative, the peak amplitude and its corresponding time were extracted in order to be compared to the theoretical amplitude and t\* for the respective model (thickness / material choice).

Since brass has the fastest diffusivity of the tested materials, it is more difficult to compute a smooth derivative. At the current length scale, incident heat from the excitation reaches the back wall very quickly and there is less time to form a stable derivative before the logarithmic time signal breaks from linearity. This can primarily be seen in Figure 2-5 where the second derivative plots aren't extremely smooth and discrete points start to become more apparent in the thinner models.

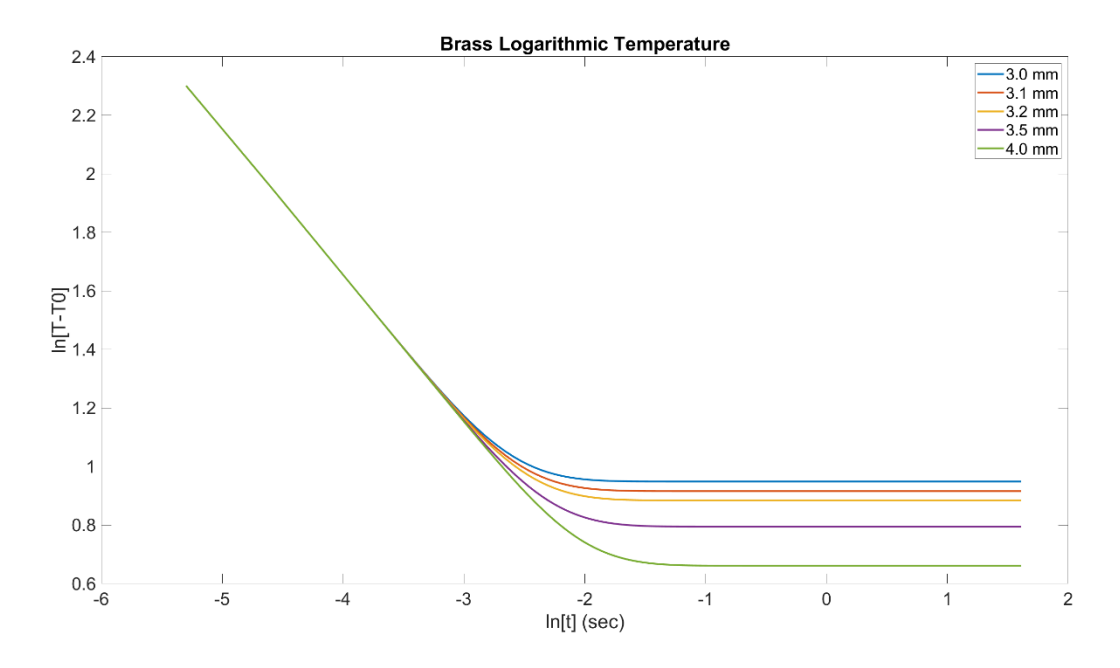


Figure 2-3: Logarithmic temperature history for brass.

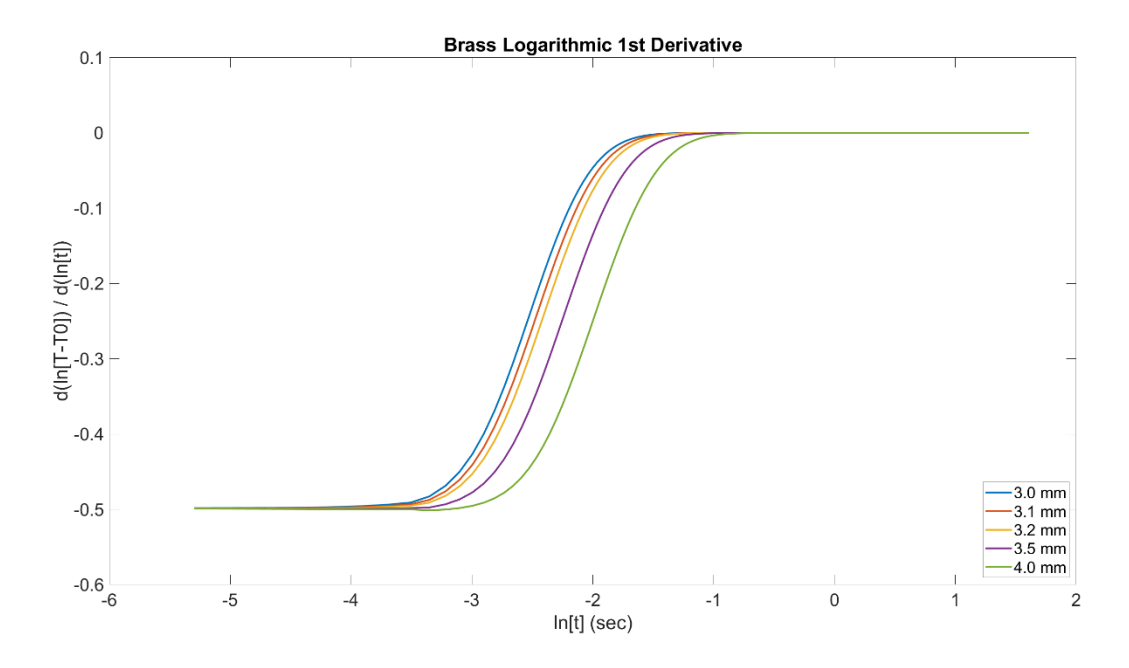


Figure 2-4: 1st Derivative for brass.

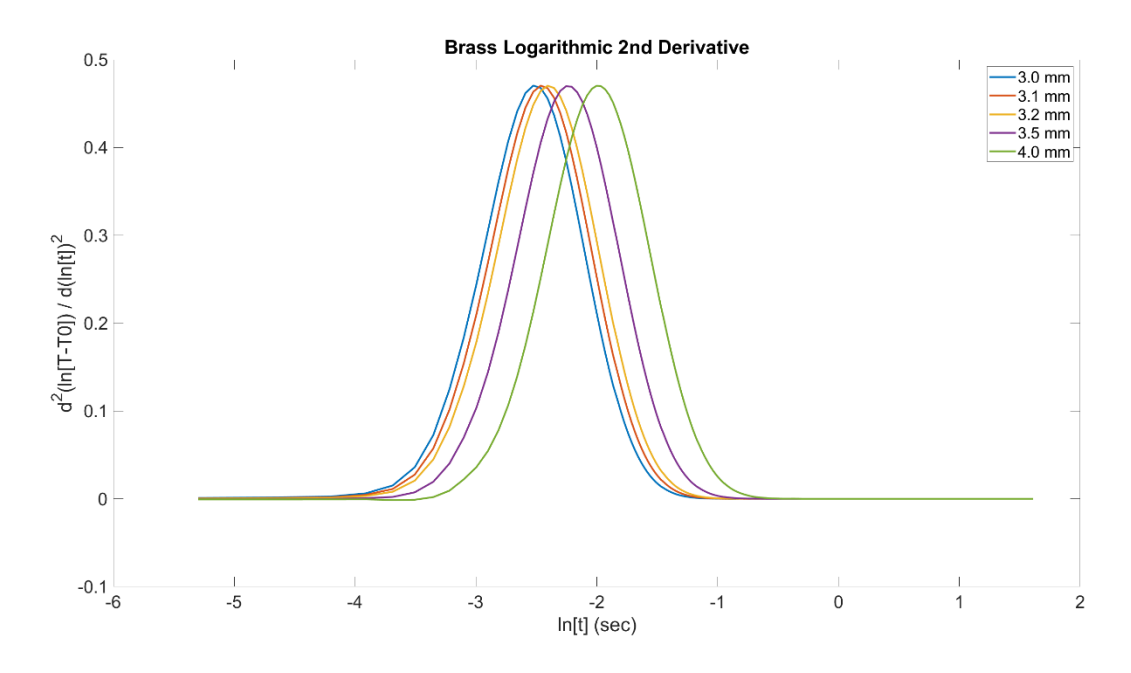


Figure 2-5: Second derivative for brass.

For steel, the diffusion process slows down (relative to brass) and forming the derivatives becomes easier and our measurement capability improves. This is primarily seen in Figure 2-8 where all second derivatives appear smooth. Figure 2-6 shows a much longer initial linear segment than brass which allows us to build the first derivative much easier due to the extra points early on which subsequently allows for a strong second derivative to be built.

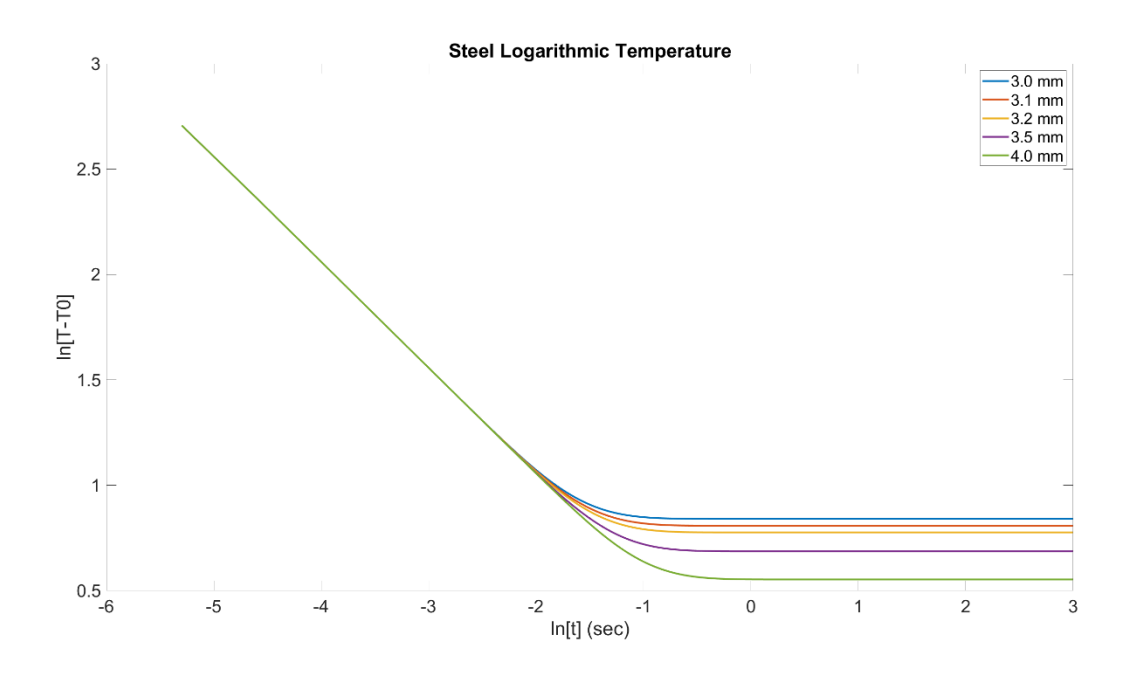


Figure 2-6: Logarithmic temperature history for steel.

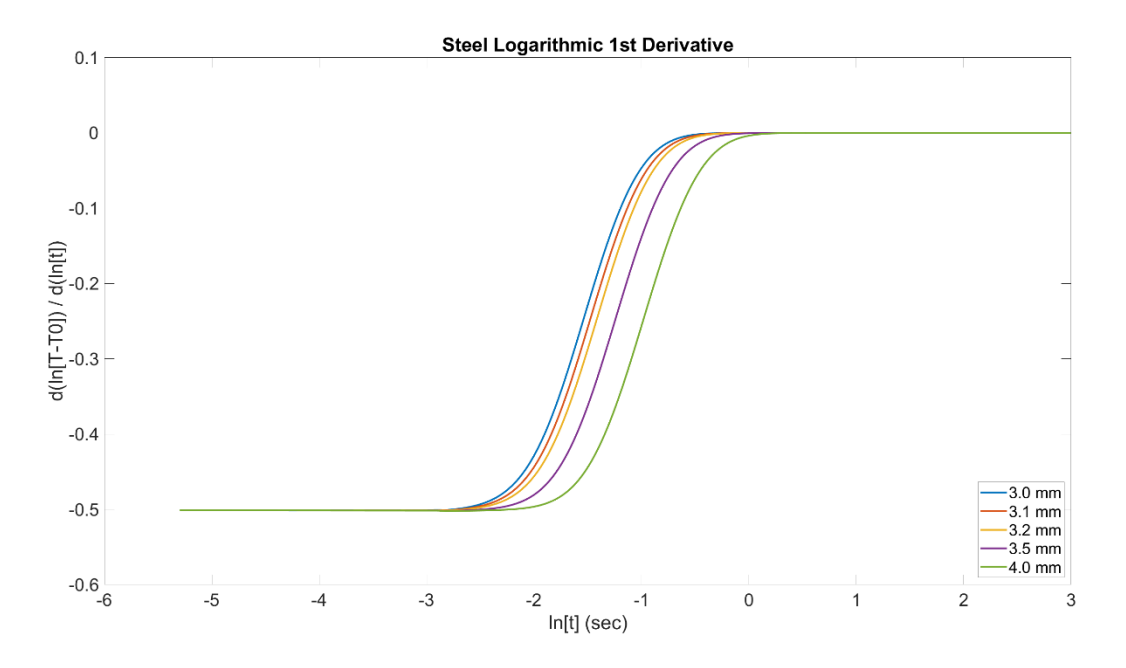


Figure 2-7: First derivative for steel.

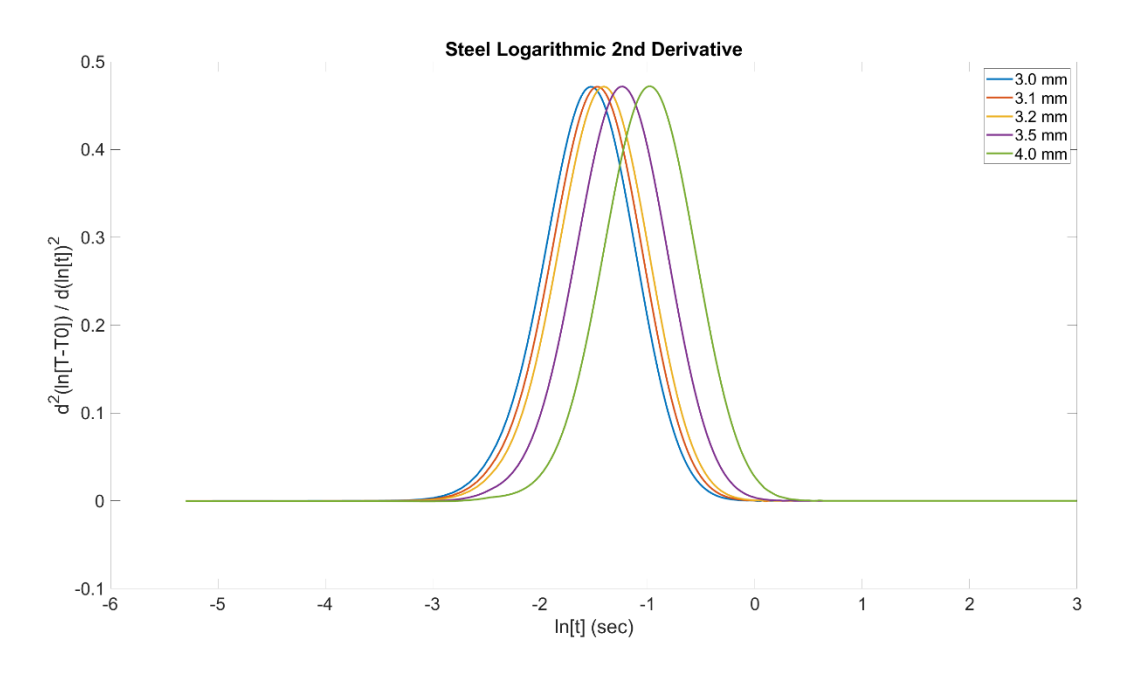


Figure 2-8: Second derivative for steel.

Finally, the composite has the smallest thermal diffusivity and therefore take the longest for heat to diffuse through the body. In this case, we obtain a very long initial linear section in the logarithmic temperature history due to undisturbed diffusion, and this can be seen in Figure 2-9. This behavior then allows for strong first and second derivatives to be built, as shown in Figure 2-10 and Figure 2-11. Figure 2-11 has a small amount of noise introduced late into the Gaussian pulse. This is due to the second diffusion step taking over. This second diffusion step is when time incrementation starts to linearly increase producing a small initial jump in time here and causing the second derivative to not be smooth at the start of this step.

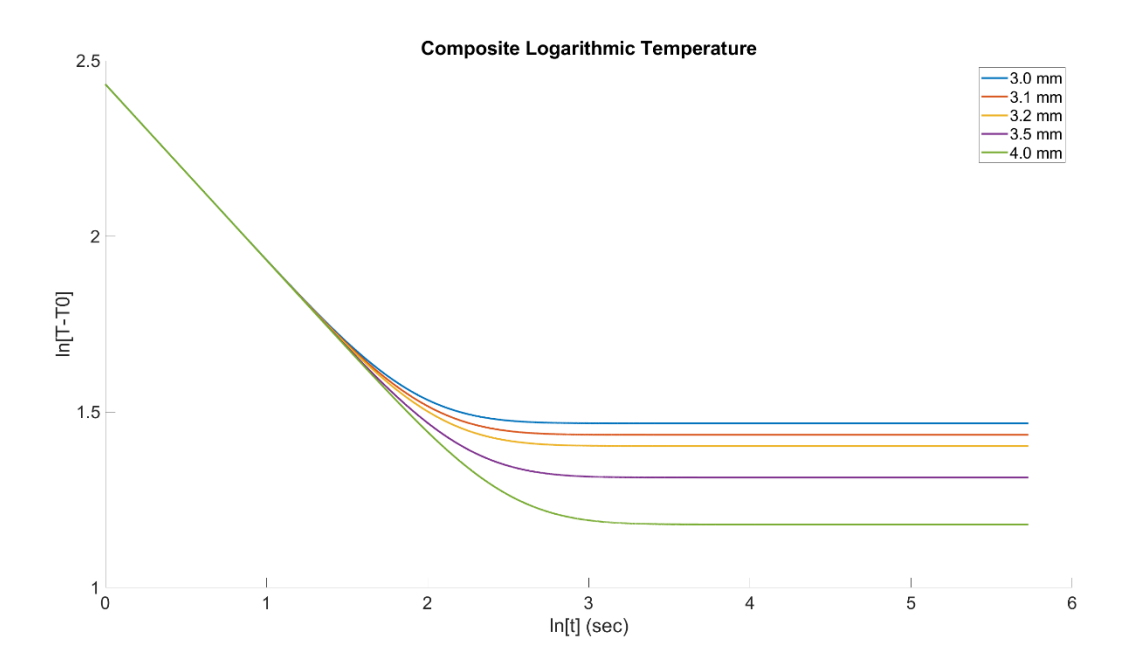


Figure 2-9: Logarithmic temperature history for an isotropic composite.

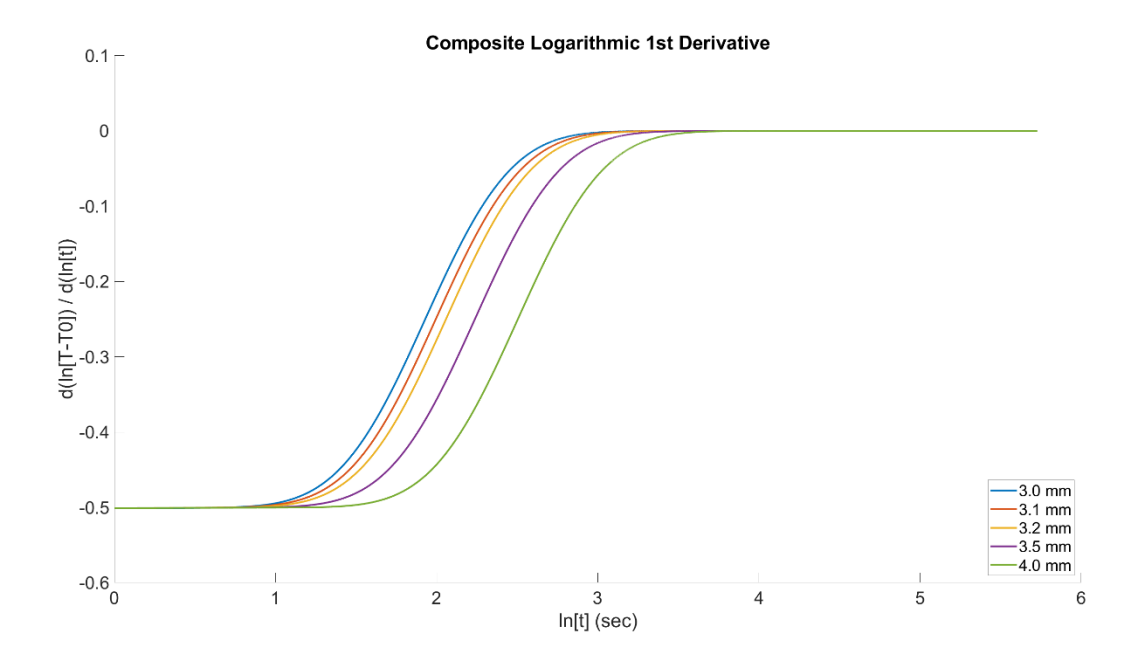


Figure 2-10: First derivative for an isotropic composite.

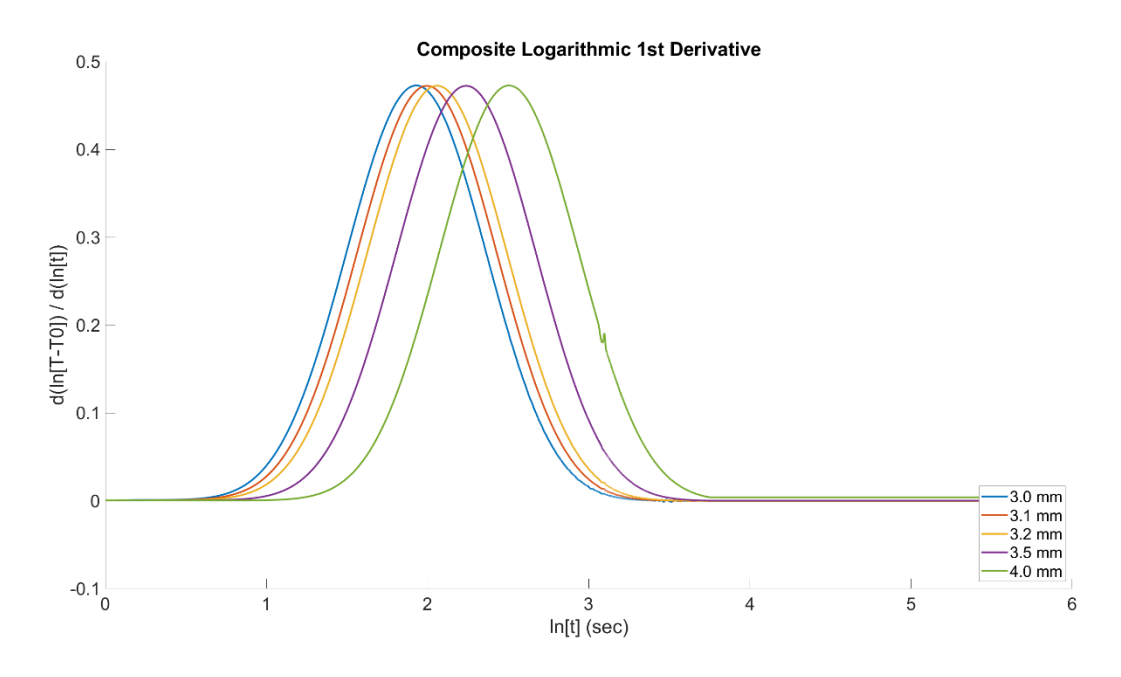


Figure 2-11: Second derivative for an isotropic composite.

The theoretical t\* is plotted for all three materials defined in Table 2-1 and compared to the t\* approximated from the developed ABAQUS® and MATLAB procedure. We see similar results as previously discussed for the plots of the different signals for brass, steel, and composite. With a very fast diffusive material, forming smooth and accurate derivatives is challenging without further reducing the time step. Subsequently, for faster diffusive materials, using this current setup yields acceptable results for t\* but at a higher error. Once the diffusion slows down and more points are obtained in the undisturbed diffusion step, smooth differentiation becomes better, and our t\* error reduces allowing us to accurately reproduce t\* through modeling. The plots for t\* for each respective material are seen below in Figure 2-12, Figure 2-13, and Figure 2-14.

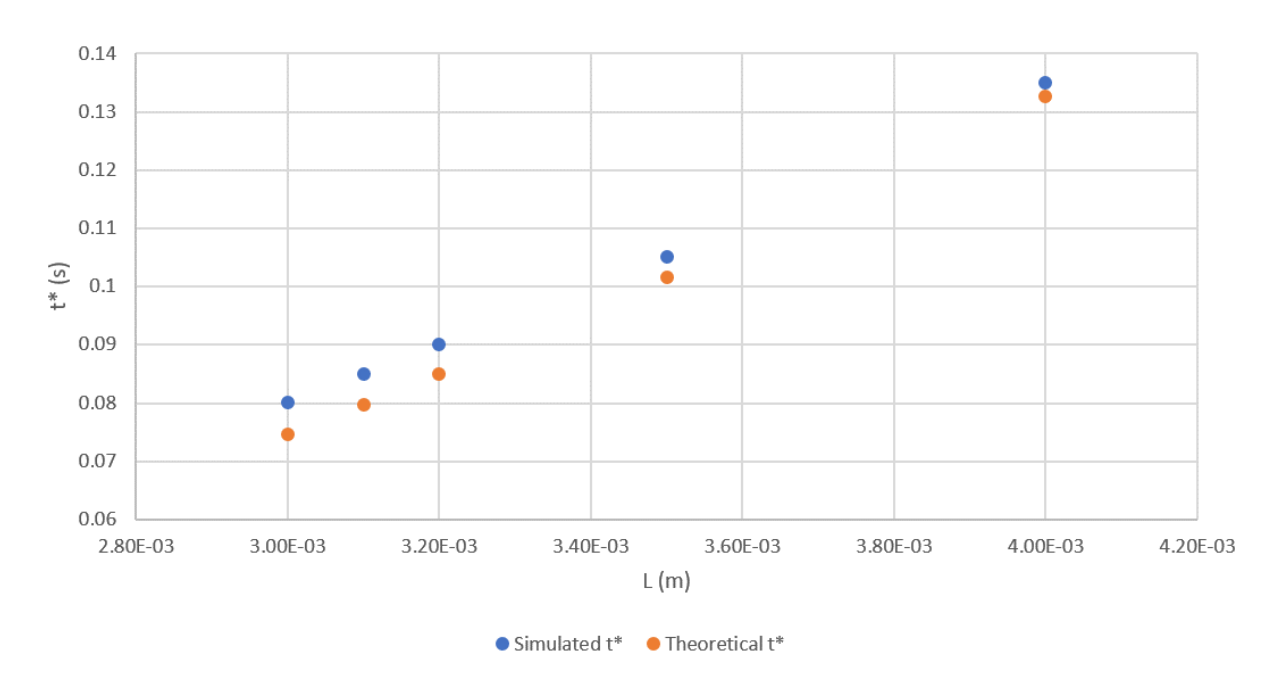


Figure 2-12: t\* across all simulated slab thicknesses for brass.

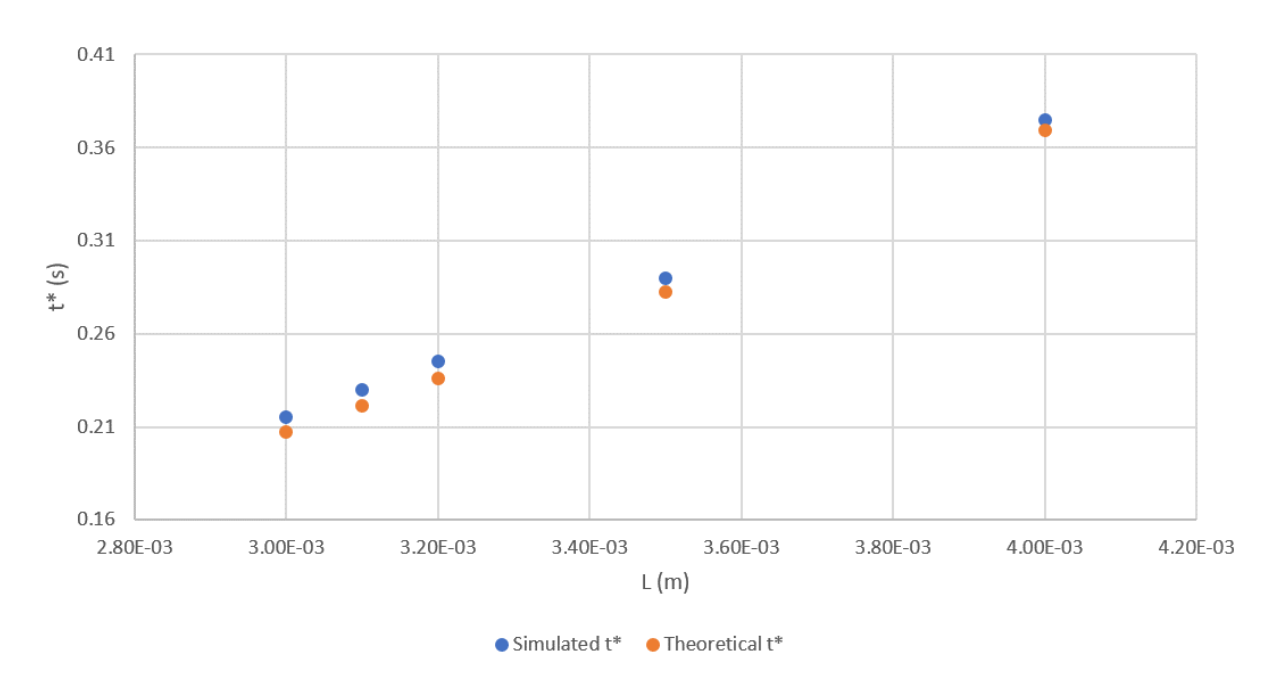


Figure 2-13: t\* across all simulated slab thicknesses for steel.

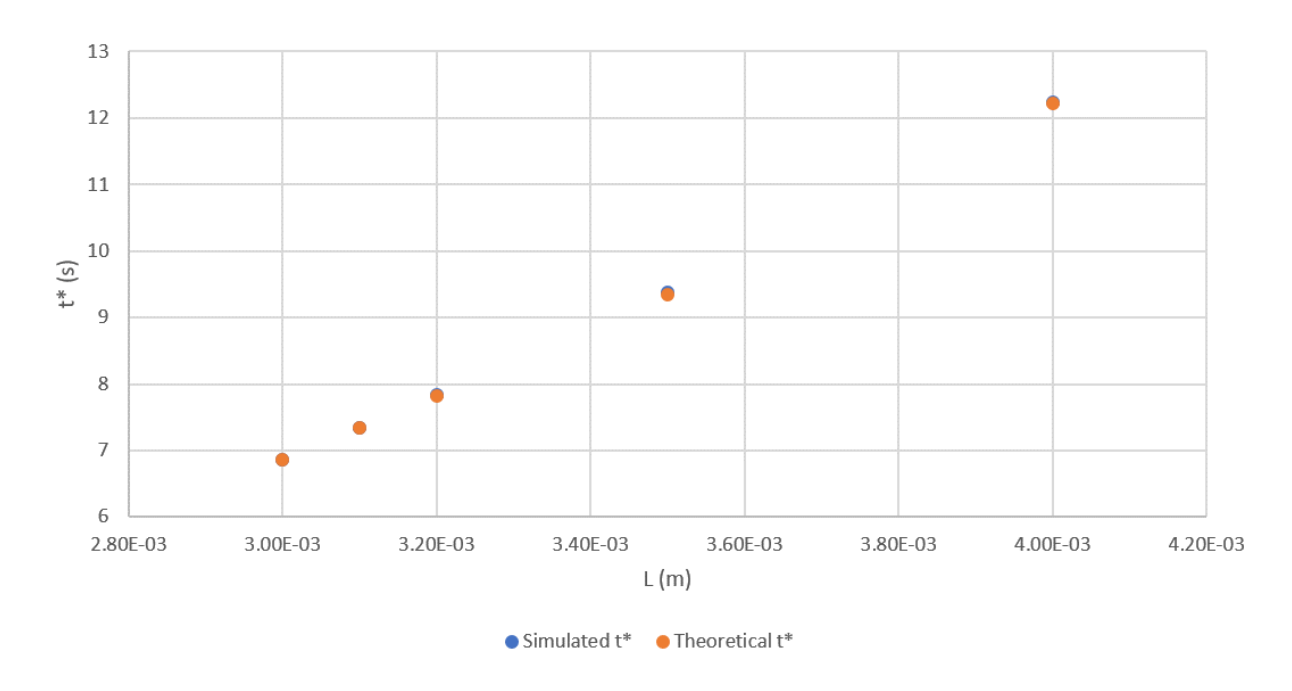


Figure 2-14: t\* across all simulated slab thicknesses for an isotropic composite.

Additionally, the peak amplitude of the 2<sup>nd</sup> derivative from numerical data was compared against the theoretical peak of 0.47, all of which line up well for all thicknesses and materials, as shown in Figure 2-15. To make the plot simpler to read, the average of the peak amplitude across the 5 simulated thicknesses were taken for each material and then compared to their theoretical values.

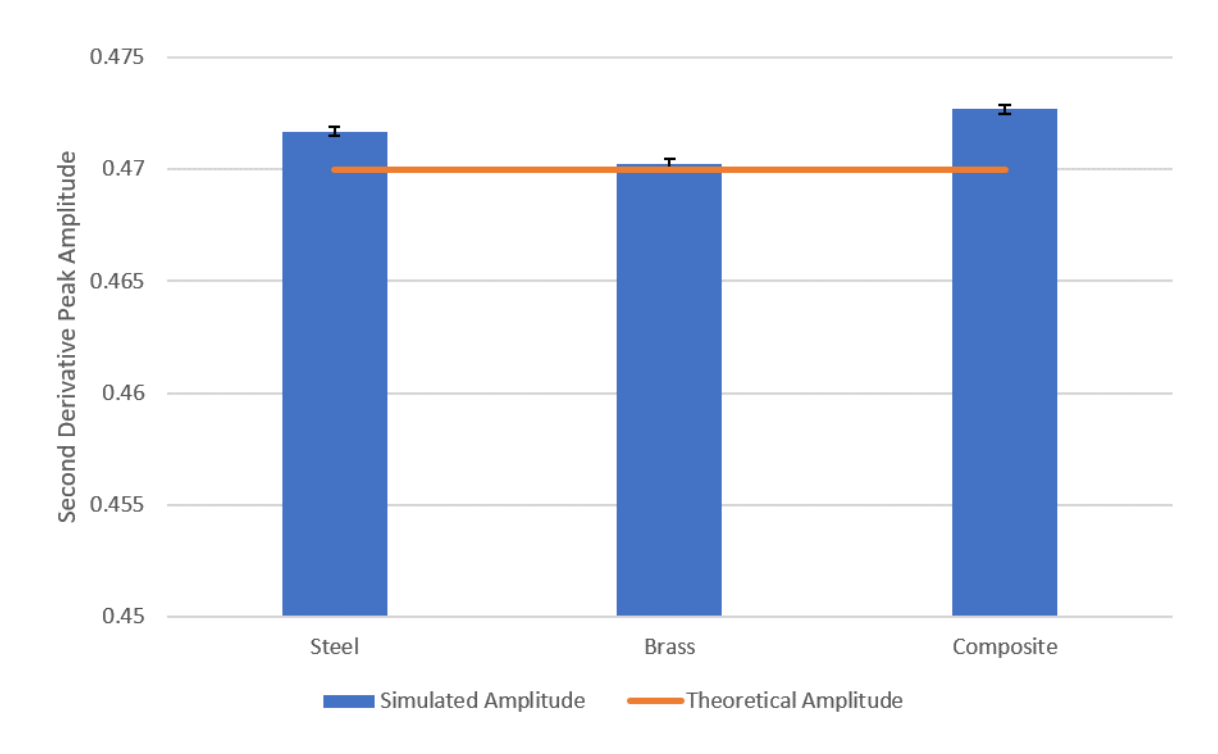


Figure 2-15: Peak amplitude comparison for all three materials.

For all three materials and across all thicknesses, the t\* and amplitude agree very well to their expected theoretical values. With a maximum error of 0.4% across the three materials, peak amplitude is very well recreated in these one-dimensional models. The creation and validation of these one-dimensional models was a vital step in creating a working model whose parameters and data processing methods can be extended to our novel work.

## Chapter 3: Two Dimensional Modeling

#### 3.1 Introduction

One-dimensional modeling provided the necessary validation to successfully recreate a known problem within finite element software. From here, the finite element model parameters (meshing, time stepping, data writing, etc.) and the data re-organization and analysis (processing workflow in MATLAB) were used as a basis to build new models. In this chapter, we seek to investigate the effect of a subsurface step geometry where the excited surface still remains smooth, but a known step size occurs at the back wall. This subsurface geometry change will cause a region of two-dimensional heat transfer where one-dimensional measurements are no longer accurate. Despite building a two-dimensional heat transfer model here, this section will not explore the mathematical background behind the two-dimensional solution. Since experimental flash thermography heavily relies on a one-dimensional approach, we will analyze the results as a deviation from the expected one-dimensional solution and use these deviations to formulate the conclusions.

#### 3.2 Model Parameters

The ABAQUS® GUI was used to create the model geometry. Instead of a uniformly thick slab, we generate various geometries with a base thickness L and a subsequent step, dL. All models were created to have a width of 120 mm such that there would be ample room to have a distinct zone of one-dimensional behavior on the thin side, a distinct transition zone where two-dimensional flow dominates, and another one-dimensional zone on the thick side. A sample schematic is shown below in Figure 3-1.

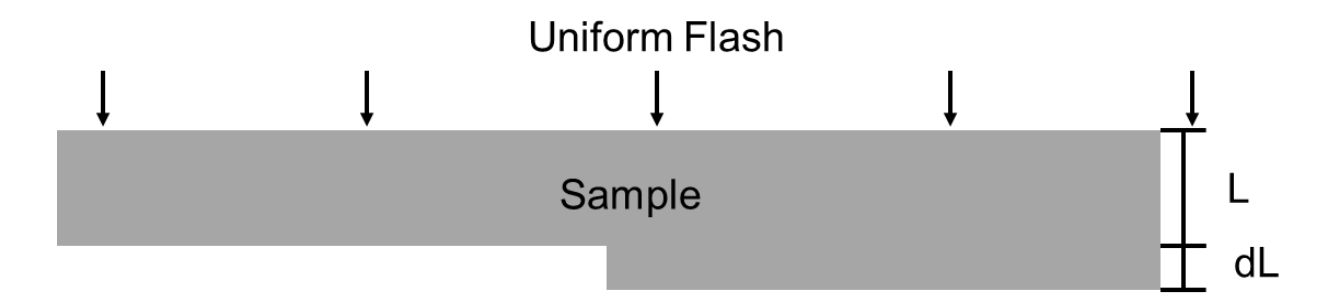


Figure 3-1: Schematic of sample geometry (not to scale).

Additionally, all surfaces were assigned adiabatic boundary conditions except the top side of the slab which is subjected to the same 1 ms heat pulse as previously defined in Chapter 2.

The model was also meshed within ABAQUS®. A procedure similar to that used for the uniform slab was employed. A mesh bias was introduced such that the element size reduced as it neared the surface of the geometry. Additionally mesh density was increased in the area surrounding the step; from -30 mm to +30 mm, the elements were defined to be 0.2 mm wide. Outside of this range, element width was increased to 0.9 mm. The mesh near the region of a step can be seen below in Figure 3-2.

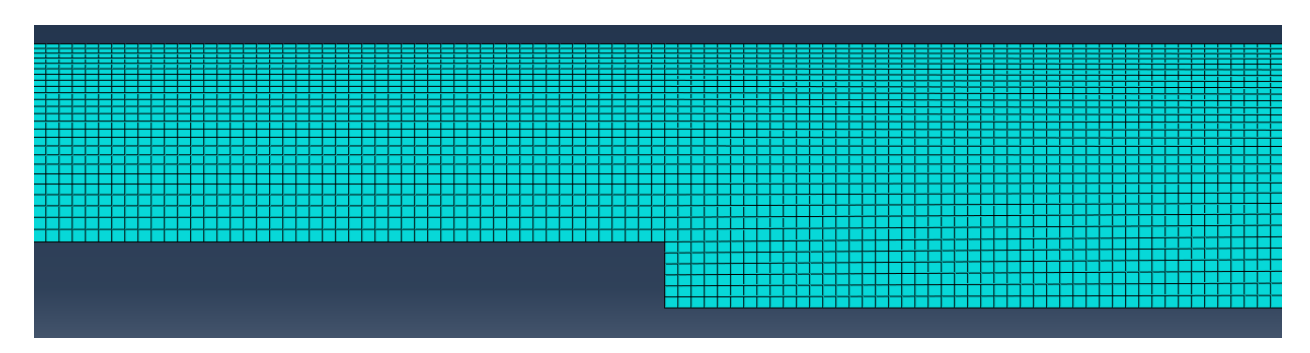


Figure 3-2: Mesh of a step geometry near the region of the step.

A parametric study was designed to investigate several combinations of base thicknesses and step sizes. Four base thicknesses were chosen, and each base thickness would be paired with 4 varying step sizes. The steps sizes (dL) were chosen such that there would be 4 combinations of

a normalized step (dL/L) for each base thickness (L). The design geometry is tabulated below in Table 3-1.

Table 3-1: Design Geometry for varying step models

L (mm)	dL 1 (mm)	dL 2 (mm)	dL 3 (mm)	dL 4 (mm)
2	0.0667	0.1333	0.3333	0.6667
3	0.1	0.2	0.5	1.0
4	0.1333	0.2667	0.6667	1.3333
5	0.1667	0.3333	0.8333	1.6667
dL/L	0.0333	0.0667	0.1667	0.3333

## 3.3 Transition Zone Definition

The transition zone is expected to be a measureable area in the vicinity of the step in which one-dimensional measurement is no longer valid due to dominant two-dimensional heat flow. We begin by examining the second derivative incrementally along the excited surface on both the thin side of the step and the thick side of the step for steel, as seen in Figure 3-3 and Figure 3-4.

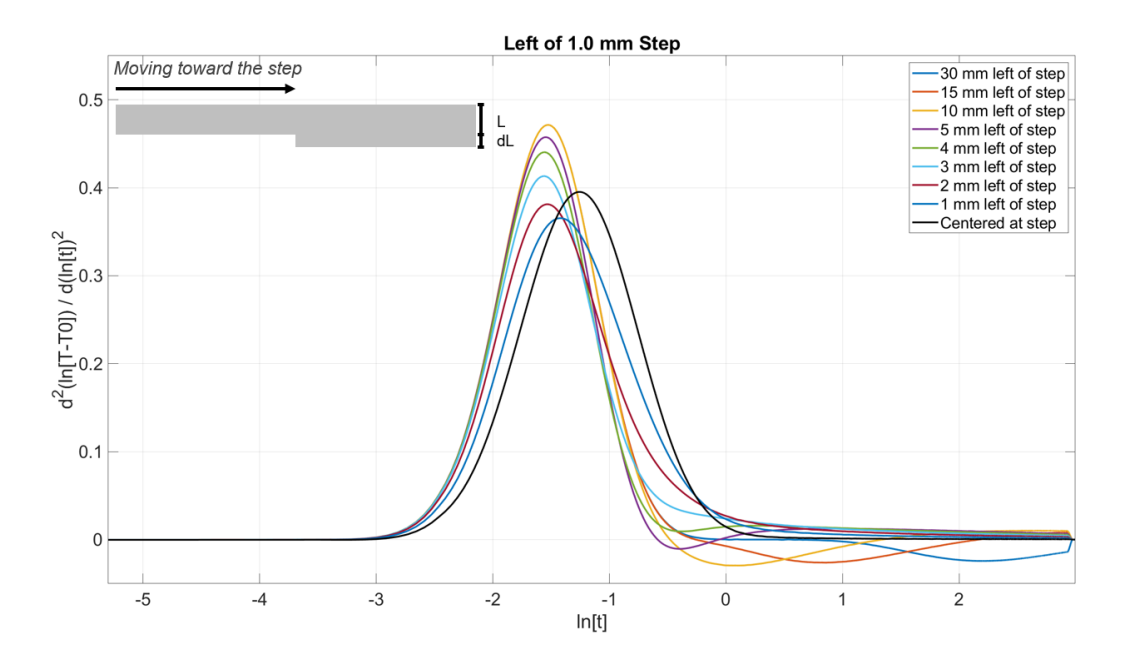


Figure 3-3: The second derivative on the thin side of a steel step (L=3 mm, dL=1 mm) at varying intervals.

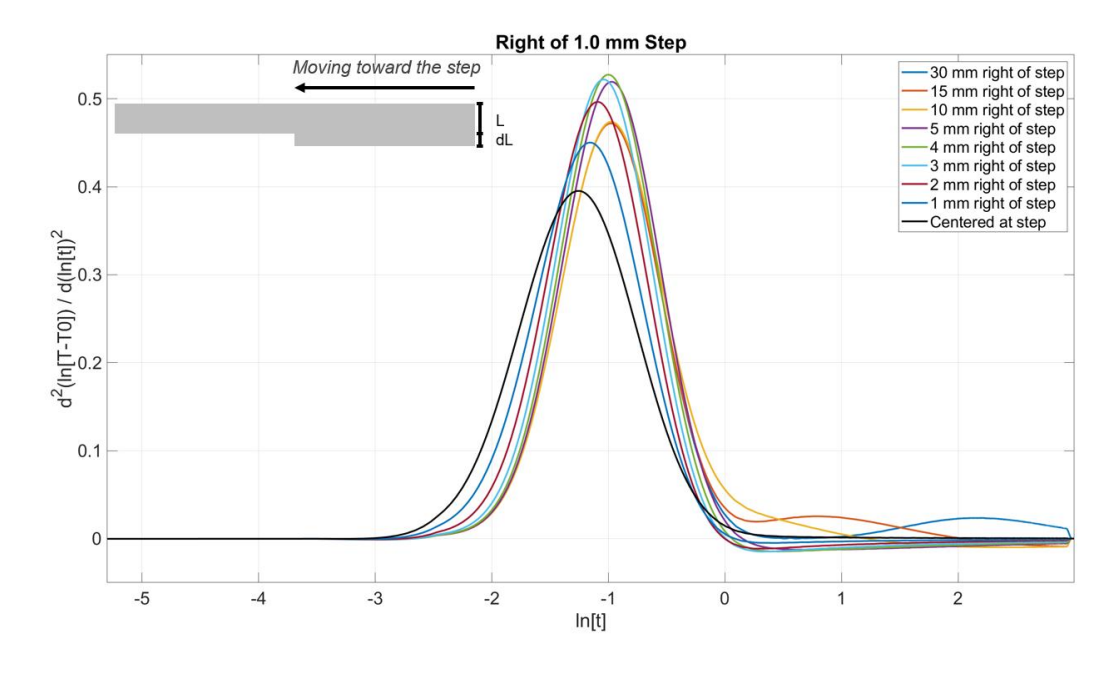


Figure 3-4: The second derivative on the thick side of a steel step (L=3 mm, dL=1 mm) at varying intervals.

Starting with Figure 3-3, we start with undisturbed one-dimensional heat transfer as all second derivatives have a value of 0. Next, we approach the Gaussian pulse where heat starts to

accumulate on the back wall and give indication of a subsurface geometric discontinuity. Finally, there is a late section in which two-dimensional flow is the primary mode of heat transfer as the derivatives dip below zero, indicating flow from the thin section of the part to the thick section of the part. By observing the peaks of the Gaussian pulse, it is evident that as we approach the step, there is both a shift in the peak amplitude that occurs and the peak time at which that amplitude occurs.

Looking at Figure 3-4, we see very similar results; one dimensional flow, a geometric discontinuity as indicated by the Gaussians, and then two-dimensional flow from thin into thick. Approaching the step from the right, there is once again a shift in both the amplitude and time at which the amplitude occurs.

What we see here is a variation from one dimensional behavior that is distinct and measurable. Since flash thermography heavily relies on the one-dimensional behavior, we are going to treat the problem as a deviation from expected one dimensional behavior and characterize its deviation. By isolating the peak amplitude along the excited surface, we can clearly see where deviation from one-dimensional behavior starts to occur. Figure 3-5 through Figure 3-7 show the variation for the four defined dL/L combinations from Table 3-1 (using L=3) across all three materials.

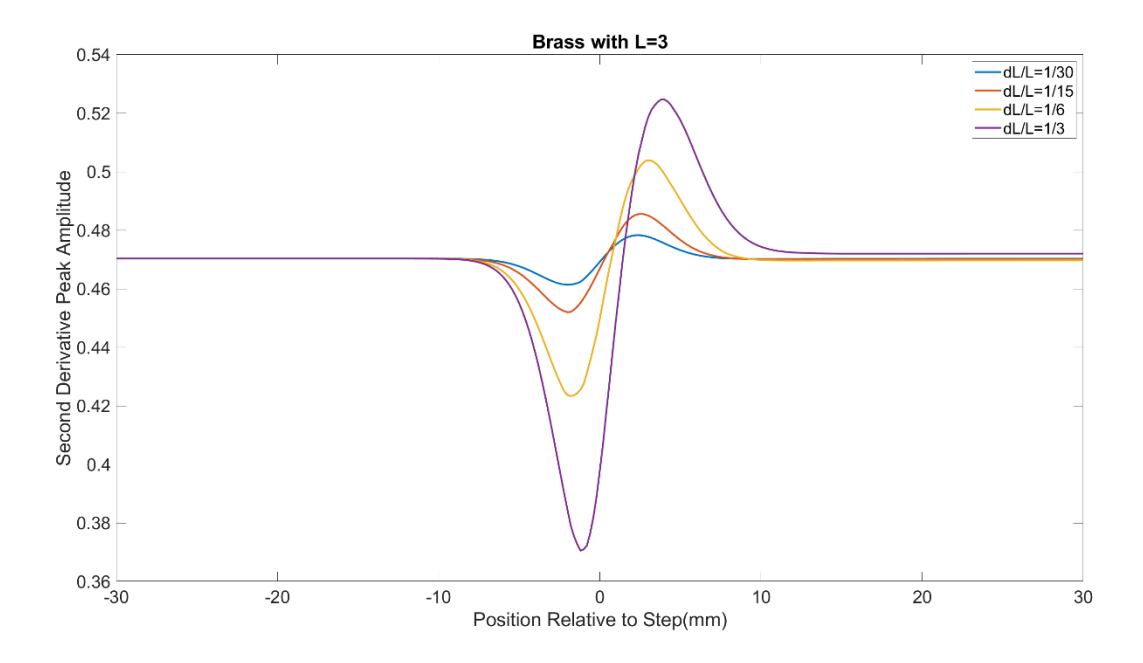


Figure 3-5: Variation in the peak second derivative amplitude across several geometries (L=3 mm) for brass.

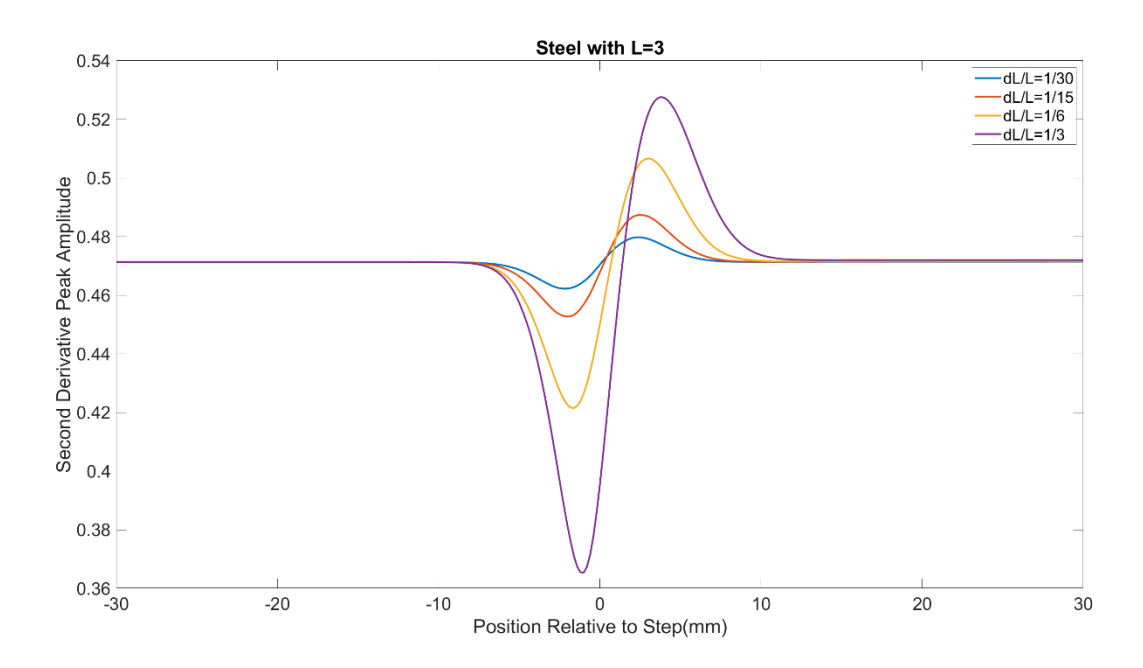


Figure 3-6: Variation in the peak second derivative amplitude across several geometries (L=3 mm) for steel.

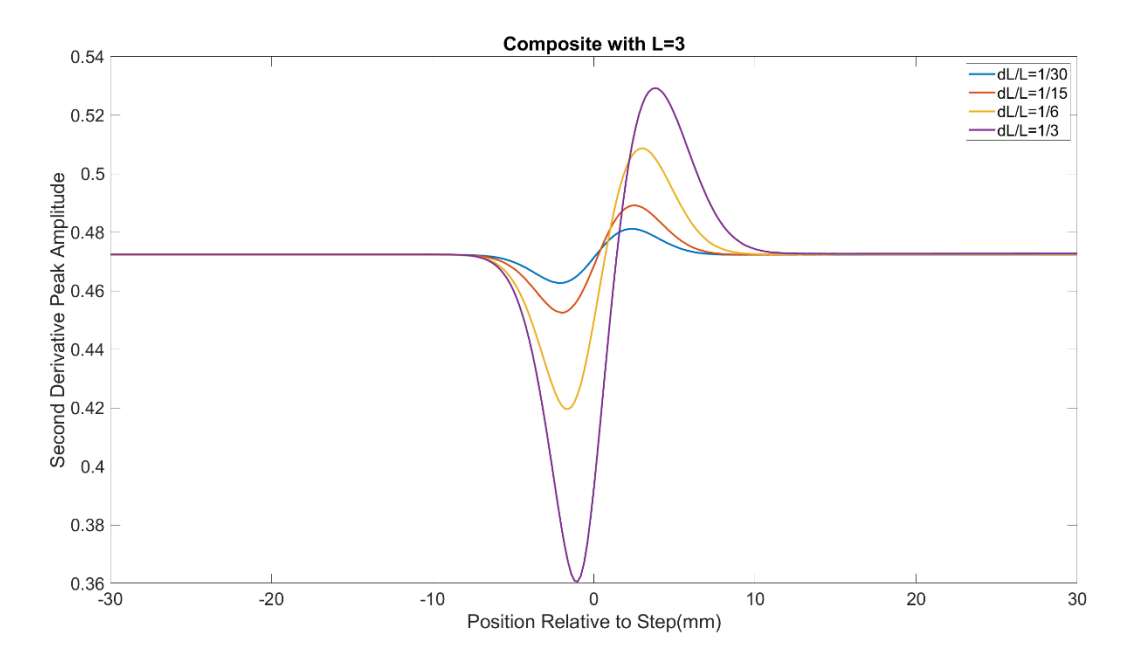


Figure 3-7: Variation in the peak second derivative amplitude across several geometries (L=3 mm) for an isotropic composite.

Across all three materials we see nearly identical deviation from one dimensional behavior for the selected geometries. This is due to removing both the dependence on the heat input and the material properties through the use of the second derivative. Additionally, we remove the dependence on the time due to diffusion by isolating the amplitudes instead of the peak time, t\*. This is a deviation from standard flash thermography practice, as t\* is more heavily favored as a measurement guideline than is the corresponding amplitude. However, using the peak amplitude easily allows us to compare across different materials and look at the problem independent of material without additional normalization of the problem through use of the Fourier Number, for example. The beauty of these plots is that they clearly show deviation from the expected value of the second derivative amplitude of 0.47 associated with the one-dimensional problem independent of material, and thus we can begin to define boundaries for a transition zone width based on the geometry alone.

Perhaps even more useful to look at are the contours of the second derivative. Figure 3-8 highlights how the peak second derivative shifts in time due to the presence of the step and shows that the transition zone expands with an increase in step size.

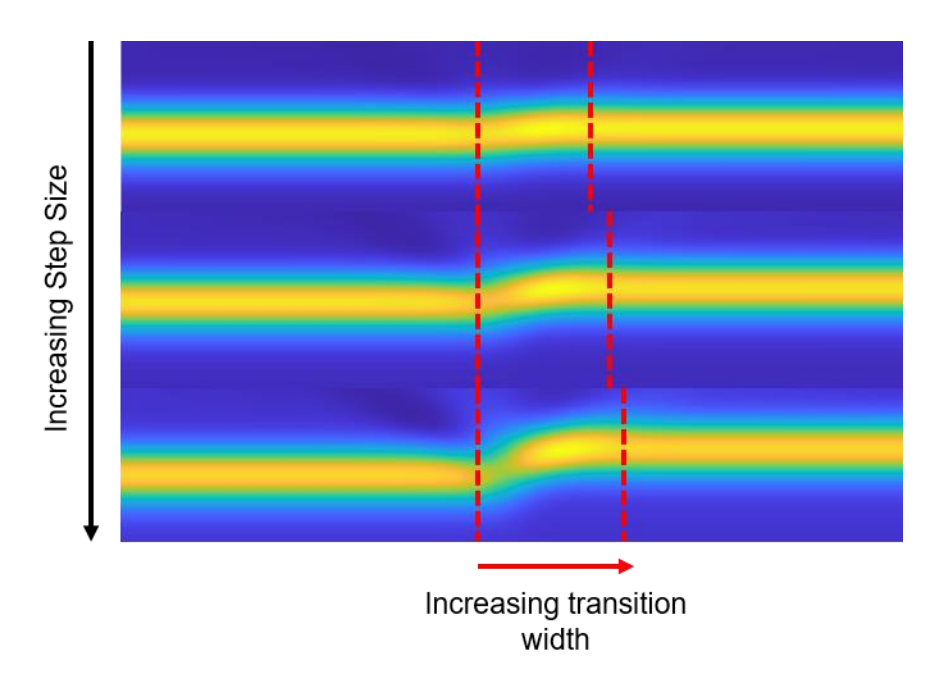


Figure 3-8: Contour plots of the second derivative with a varying step size.

To determine the width of the transition zone, we start by highlighting that the curves individually appear to be a sum of two Gaussian pulses; one negative pulse and one positive pulse. MATLAB is used to curve fit a two pulse Gaussian to each individual plot of the second derivative peak amplitude for all materials across all possible geometries based on Equation 3.1. The peak second derivative amplitude was shifted down to 0 before applying the fit.

$$y = \frac{c_1}{b_1 \sqrt{2\pi}} e^{-(x-a_1)^2/(2b_1^2)} + \frac{c_2}{b_2 \sqrt{2\pi}} e^{-(x-a_2)^2/(2b_2^2)}$$
3.1

The curve fit appropriately fits the sum of a positive and negative Gaussian pulse to the peak second derivative amplitude data. Both an example of a fit and how the sum of the fits work are shown below in Figure 3-9 and Figure 3-10.

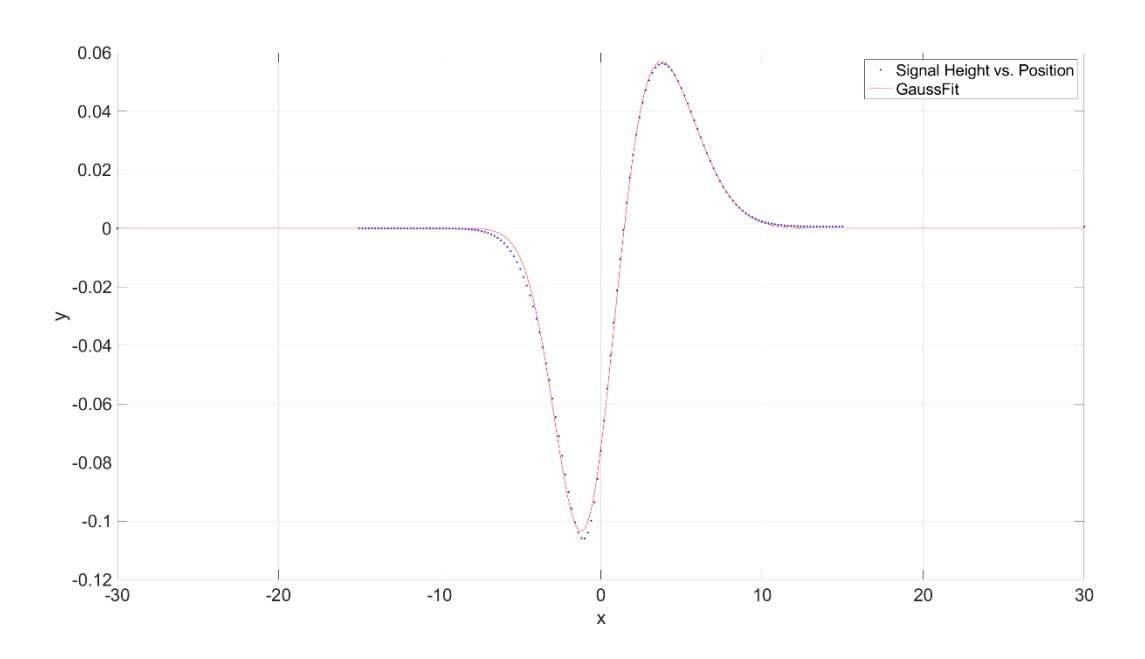


Figure 3-9: Curve fit to peak second derivative amplitude data for steel with L=3 mm and dL=1 mm.

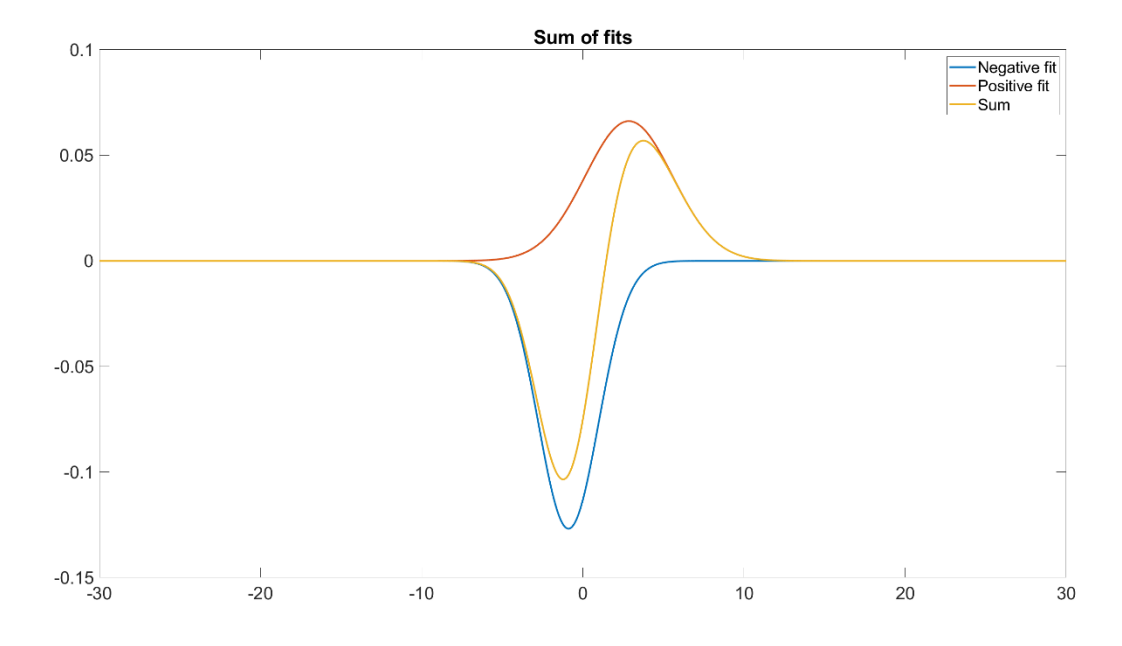


Figure 3-10: Sum of a negative and positive Gaussian pulse to form the curve fit of the peak second derivative amplitude data (L=3 mm, dL=1 mm).

Utilizing the positive and negative portions of the curve fit, it was simple to define boundaries by using the mean and standard deviation of each respective fit. To define the

positive boundary, the mean plus three standard deviations was used. For the negative portion, the mean minus three standard deviations was used. Taking the difference of the determined boundaries yields a finite width of the transition zone. This method was applied across all materials and geometry configurations.

#### 3.4 Results and Discussion

With finite boundaries defined, all geometry configurations and transition zone widths were tabulated in Excel for all three materials. A multivariate regression was applied to the entire dataset to create a predictive equation for the transition zone width based solely on the geometry of the material. It was found that the transition zone width has a linear relationship to both the base thickness (L) and the step thickness (dL) which remains independent of the material properties or heat input. A plot of the regression vs. the transition zone width data is shown below in Figure 3-11 to highlight the goodness of fit of the multivariate regression.

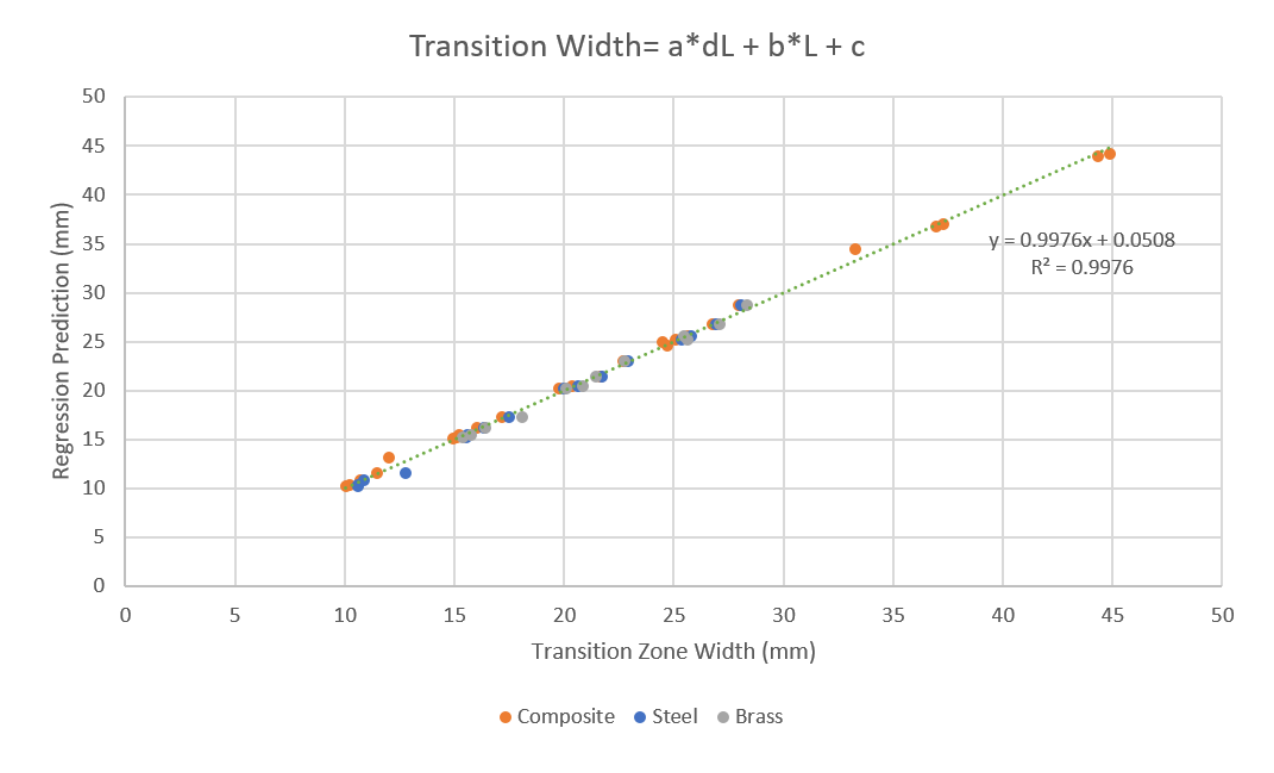


Figure 3-11: Transition zone width regression model across all tested geometries and materials.

Additionally, the model parameters are tabulated in Table 3-2 with Equation 3.2 following.

Table 3-2: Model parameters for transition zone width fit equation

a	b	c
2.33572	4.91039	0.26352

$$Trans_{width} = 2.33572(dL) + 4.91039(L) + 0.26352$$
 3.2

It is worth noting that the composite has extra data points for the transition zone width that extend out past the defined geometries from Table 3-1. These additional geometries were chosen at random to test the validity of the modeling outside the simple chosen boundaries and to see if the model breaks down at higher transition zone widths or becomes nonlinear. Our results do not show any nonlinearity being introduced with growing transition zones, however, it does become apparent that the transition zone width may end out being larger than possible manufactured

parts due to the heavy larger dependence on the base thickness. While these current results only highlight the finite width of the transition zone, we also see that, with increasing widths due to thicker geometries, the transition zone is no longer centered on the step. With increasing step thicknesses, the transition zone shifts toward the thick side of the step due to the increased dominance of two dimensional heat transfer from the thin side to the thick side of the step. However, this work doesn't go into the shifting of the transition zone or prediction of how the center of the zone may move simply because our main interest relates to small steps in the applications of composite materials.

# Chapter 4: Limits of Step Detectability

#### 4.1 Introduction

As with any modeling, there is oftentimes a set of unrealistic and idealized assumptions made that do not necessarily transfer well to a practical experiment. The previously described modeling employs adiabatic boundary conditions on all exposed surfaces (except during the excitation phase) and while it is possible to insulate a sample well in an experiment, recreating an adiabatic boundary is not practical. So far, this work has defined a transition zone based purely on sample geometry. However, a sensitivity limit exists in practice that does not exist in modeling, which would impact the ability to detect a step and thus impact the realistic effects from a transition zone created by the subsurface step. Common infrared (IR) cameras, such as the FLIR A6751, have a static detection limit of 20 mK [16]. Since previous analysis did not take raw temperature data into consideration, this chapter will provide two different expressions that can be used to predict the detectability of a step derived from the adiabatic solution (Equation 1.4). The derived equations utilized in combination with a camera's detection limits can be used to provide insight into what kinds of steps may be detectable.

#### 4.2 Detectability Equation

Since a primary measurement method utilizes t\*, we will begin deriving an equation for detectability based on the temperature at time t\*. By substituting Equation 1.5 into Equation 1.4 we arrive at a simplified temperature equation on the thin side of the step as:

$$\Delta T(t_1^*) = \frac{Q}{\rho CL} \left[ 1 + 2 \sum_{n=1}^{\infty} e^{-n^2 \pi} \right]$$
 4.1

From here, we know that the infinite sum of a decaying exponential is a converging sum and we can redefine the equation as:

$$\Delta T(t_1^*) = \frac{Q}{\rho CL} [1 + 2A] \tag{4.2}$$

where *A* is the value of the infinite sum.

Similarly, for the thick side of the step:

$$\Delta T(t_2^*) = \frac{Q}{\rho C(L + dL)} [1 + 2A]$$
 4.3

At this point, we can simply take the difference of Equation 4.2 and Equation 4.3 to obtain:

$$T(t_1^*) - T(t_2^*) = \frac{Q}{\rho C} [1 + 2A] \left( \frac{1}{L} - \frac{1}{L + dL} \right)$$
 4.4

We can make this equation a bit neater with some algebraic manipulation of the term containing the thickness measurements and arrive at:

$$T(t_1^*) - T(t_2^*) = \frac{Q}{\rho C} \frac{dL}{L(L+dL)} [1 + 2A]$$
4.5

Utilization of Equation 4.5 along with known camera characteristics will give some insight into what types of steps should be easily detectable given the known material properties, geometry, and heat input.

Another possible measurement would be to use the final steady state temperature to define a detectability limit. To accomplish this approach, we start by taking the limit as time goes to infinity of the adiabatic solution for the thin side of the step.

$$\lim_{t \to \infty} (\Delta T_1(t)) = \frac{Q}{\rho CL}$$
 4.6

We can perform the same limit but now for the thick side of the step:

$$\lim_{t \to \infty} (\Delta T_2(t)) = \frac{Q}{\rho C(L + dL)}$$

$$4.7$$

Once again, we can simply take the difference of Equation 4.6 and Equation 4.7 to arrive at a steady state temperature difference:

$$T_1 - T_2 = \frac{Q}{\rho C} \left( \frac{1}{L} - \frac{1}{L + dL} \right) \tag{4.8}$$

Performing the same algebraic manipulation on the term containing the thickness measurements simplifies the equation to:

$$T_1 - T_2 = \frac{Q}{\rho C} \frac{dL}{L(L + dL)} \tag{4.9}$$

Similarly, utilization of Equation 4.9 along with the camera characteristics should be useful in predicting what types of steps should realistically be detected.

#### 4.3 Results and Discussion

Direct comparison of Equation 4.9 and Equation 4.5 show extreme similarity. The only difference is that Equation 4.5 is exactly Equation 4.9 but multiplied by approximately 1.08 due to the infinite sum term appearing in Equation 4.5. Either equation will work, however, Equation 4.5 is going to be the more conservative approach since it will provide a greater temperature difference for its threshold. Even though the analysis was done based on a purely adiabatic scenario, the resulting equations yield the maximum possible detectable temperature difference and give a best case scenario in experiment. If a predicted temperature drop across a step is below or near to the camera's static detectability limit, we would expect to be unable to accurately distinguish the steps from one another or accurately measure whatever transition zone may arise from the two-dimensional flow in this region. It is also important to note that a camera's detection limit is defined statically. In a sample where a subsurface geometry change initiates a two-dimensional heat flow, the problem is very much dynamic. Using a temperature

measurement at t\* or even at its steady state limit, may still be lower than predicted simply due to the transient nature of the problem.

To get a better intuition of how detectability might vary across geometries and materials, surface plots were generated from Equation 4.5 for the materials listed in Table 2-1 for a heat flux value of  $12 \text{ kJ/m}^2$  in the figures below.

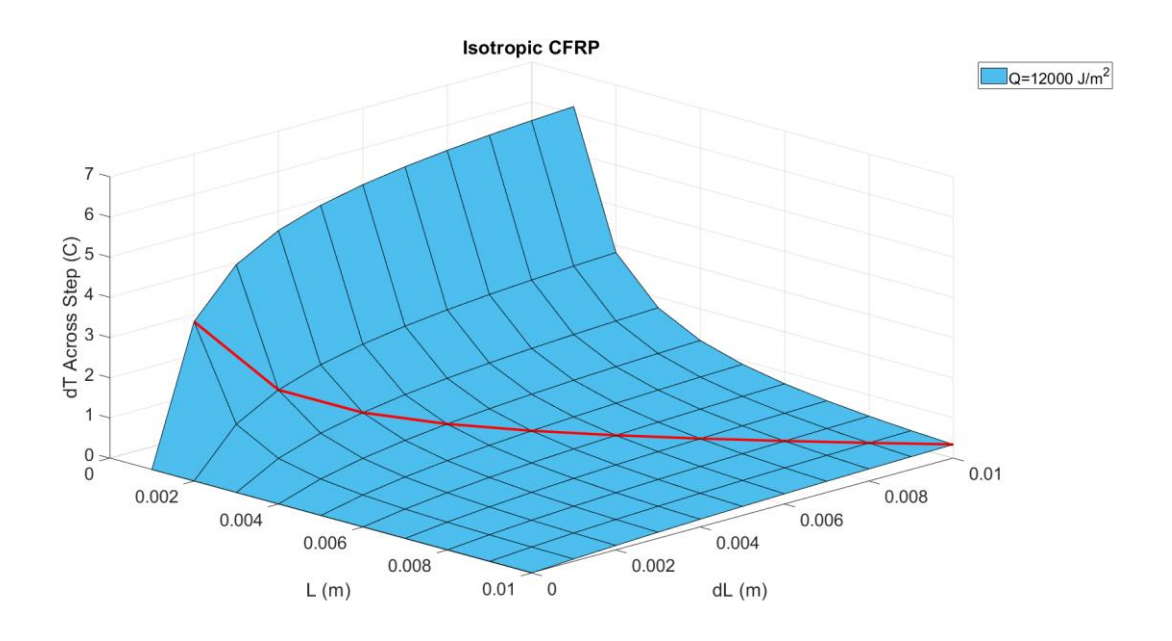


Figure 4-1: Temperature drop across a step for an isotropic carbon fiber material.

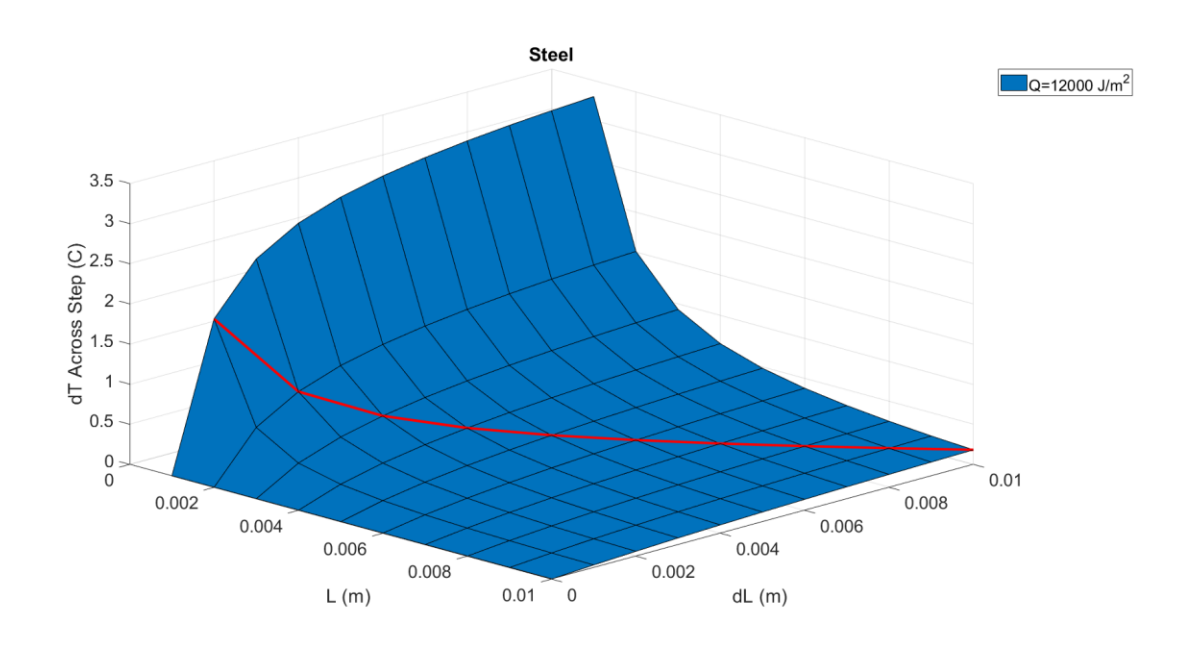


Figure 4-2: Temperature drop across a step for a low carbon steel.

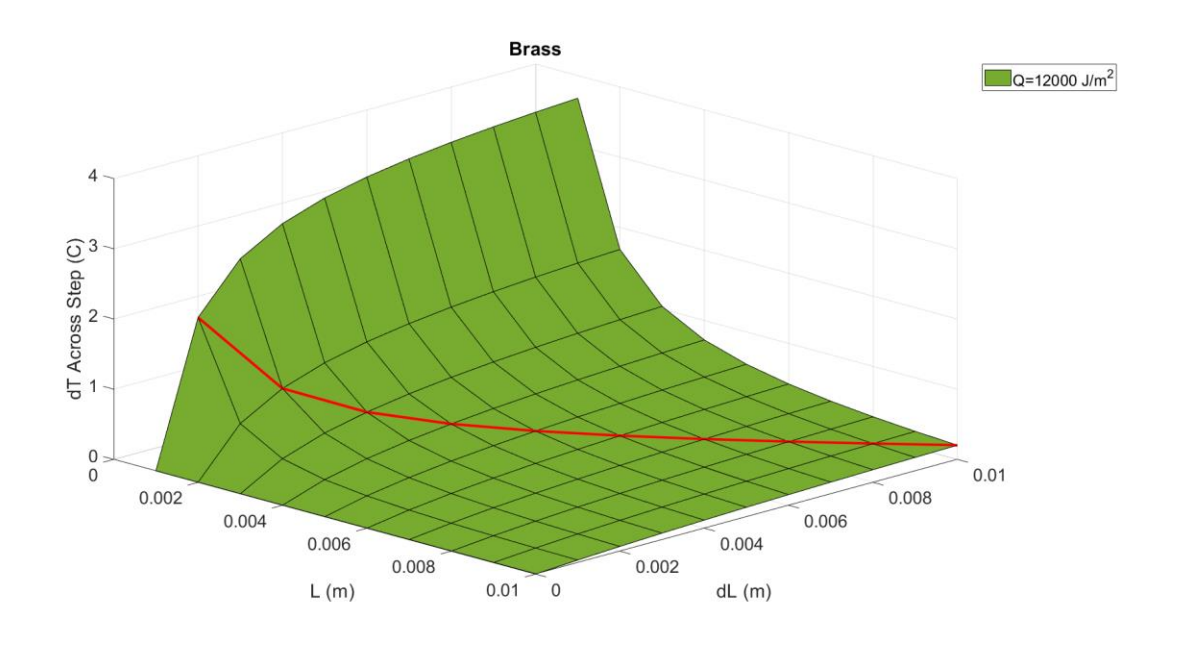


Figure 4-3: Temperature drop across a step for brass.

From Figure 4-1 through Figure 4-3, we can see that the most easily detectable steps are those which have a small base thickness (L) and a large step size (dL). However, the geometries that are most likely going to be studied are those wherein dL<L which is shown graphically by

the lower part of the images separated by the red line. These types of geometries are more interesting to study since the corresponding temperature drops across a step are closer to the detectability limit for the camera, and guidance in this regime is needed.

# Chapter 5: Experimental Validation of Model Predictions

### 5.1 Introduction

The goal of the modeling was to create a prediction for how a subsurface geometry change would affect the ability to use flash thermography as a measurement method near the presence of a step. In order to test a predictive model, an experiment needs to be designed. The goal of the experiment is to test the validity of Equation 3.2 and if needed, iterate on either modeling or experiments in order to reach a unified conclusion. In doing this, we hope to guide future experiments in which a subsurface step is present so that experimentalists can properly determine the presence and effects of a step and also distinguish it from other possible defects. Conversely, critical components that need constant inspection can be 'designed for inspectability" such that any sub-surface step geometry can be selected to meet the detectability limits.

## 5.2 Steel Plate Design

In order to test and validate the model predictions, a steel plate was designed based on the regression model defined in Equation 3.2. The step sizes were chosen such that we could achieve small step sizes while maintaining proper manufacturability and to test thickness combinations that were simulated and also those that were not. The design geometry and the manufactured plate can be seen below in Figure 5-1 and Figure 5-2.

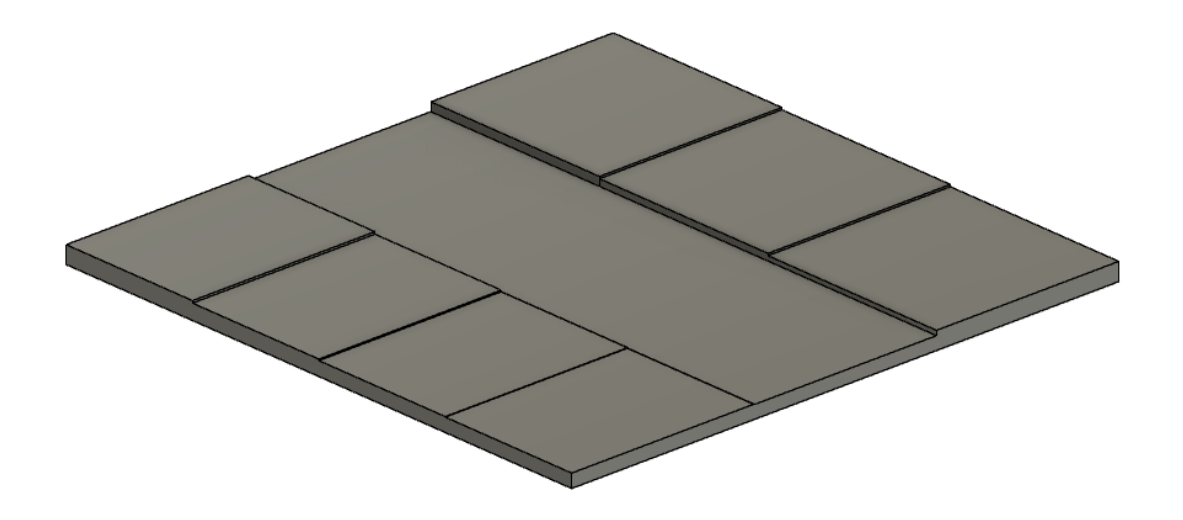


Figure 5-1: Modeled Geometry.



Figure 5-2: Machined Steel Plate.

Additionally, to compare the design geometry to the final machined geometry, a comparison between the machined geometry of the steps and the design geometry is included below in Table 5-1. While the machined geometry sometimes varies quite a bit from what was designed, the importance is that each section can be properly measured and we can use those thickness measurements in theoretical calculations to compare with real measurement.

Table 5-1: Machined geometry vs. designed geometry

Machined (mm)		Designed (mm)	
L	dL	L	dL
4.88	0.28	5.00	0.17
4.88	0.46	5.00	0.33
4.88	0.97	5.00	0.83
4.88	1.63	5.00	1.67
4.88	1.93	5.00	1.78
4.88	2.71	5.00	2.54
4.88	3.38	5.00	3.30
5.16	0.18	5.16	0.17
5.33	0.51	5.33	0.50
5.84	0.66	5.83	0.83
6.81	0.77	6.78	0.76
7.58	0.67	7.54	0.76

Use of Equation 3.2 allowed the plate to be designed such that there would be stable, one dimensional areas on each step of the plate such that a distinct transition zone should be capable of being measured, without transition zones overlapping from other steps. With this design, there are a total of 12 transition zone measurements that could be measured and compared to the prediction. There are 7 total transition zones defined across "parallel steps" and an additional 5 across "series steps." Parallel steps are defined as a sequence where there is only a single step from thin to thick. Series steps are defined as a sequence where there are multiple steps, similar to a set of stairs. Both orientations can be seen in Figure 5-3.



Figure 5-3: Schematic of parallel steps and series steps.

Lastly, it is important to note that the plate was designed solely on information from Equation 3.2 and insight taken from Chapter 4, and the detectability requirement for steps was not considered at this time.

## 5.3 Data Analysis

Data was acquired using a commercial Flash Thermography system [17], including a camera operating at 120 Hz and xenon flashlamps. The data was processed using Thermographic Signal Reconstruction (TSR) in the system Virtuoso software. In Virtuoso, the first derivative inflection point was exported as a .dat file and input to MATLAB for further analysis. Here, the first derivative inflection point was used instead of the maximum of the second derivative because it gives a near identical way to reproduce t\* but uses less mathematical operations on the data, and therefore reduces the error incurred from subsequent calculus.

In MATLAB, the .dat file is loaded in, the dataset is cropped, and then scaled from pixels to inches as seen in Figure 5-4.

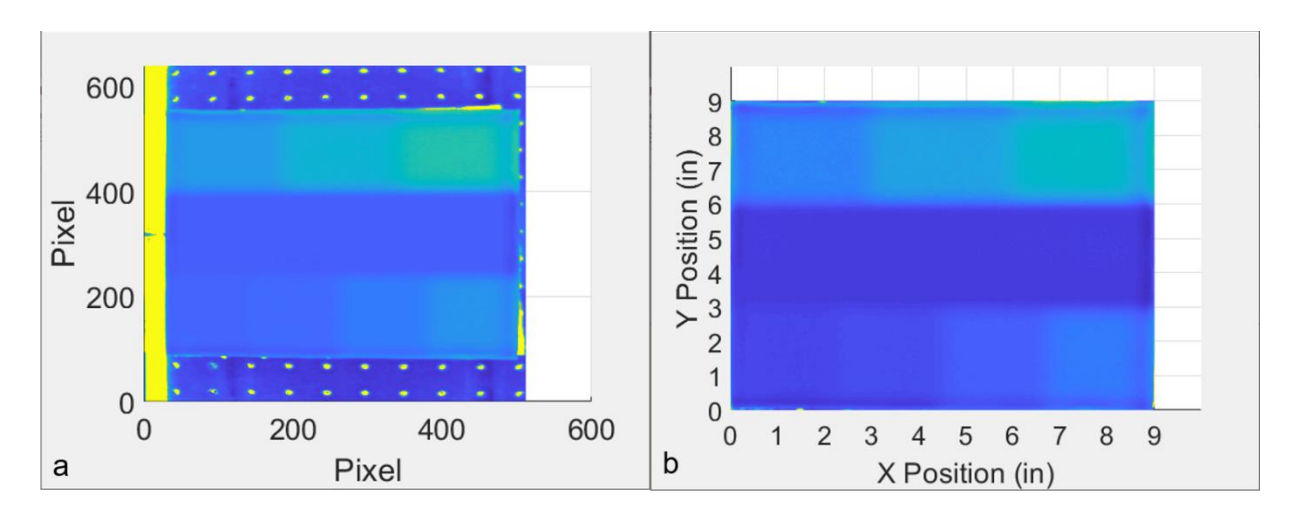


Figure 5-4: Raw data in MATLAB in a) pixels and b) inches.

Next, the data was processed by taking 9 varying cross sections, at the center of each step for 7 parallel steps and 2 along the each series orientation, as shown in Figure 5-5. Finally, each

cross section was split into individual areas in order to isolate the thirteen transition zones within their own dataset.

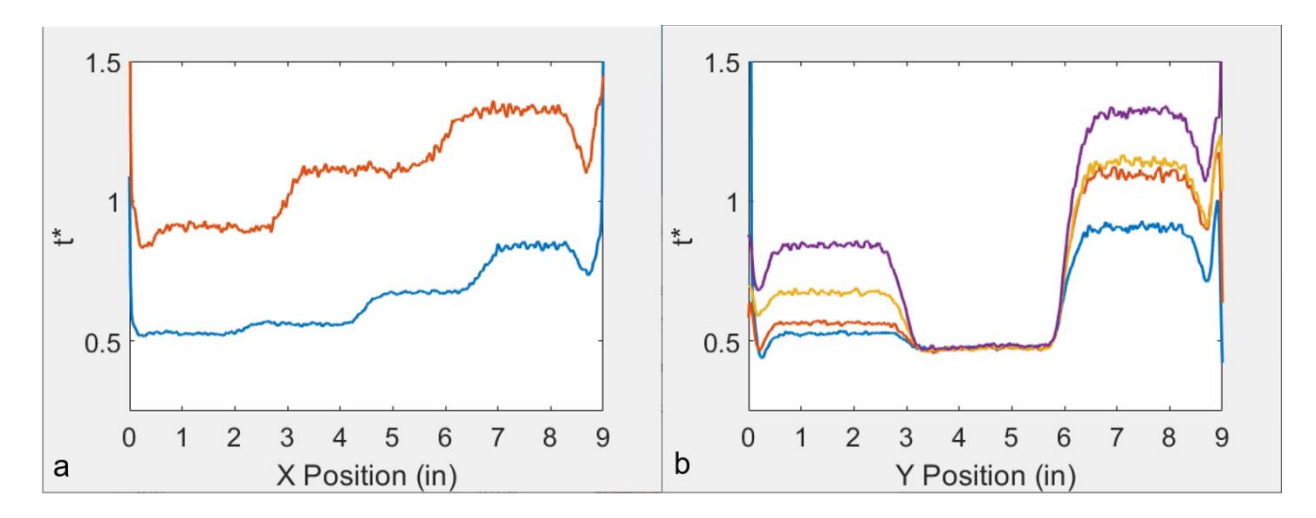


Figure 5-5: a) Data taken from the series orientations and b) data taken across all parallel orientations.

A visual representation of how the data cross sections were extracted from the scaled dataset can be seen below in Figure 5-6.

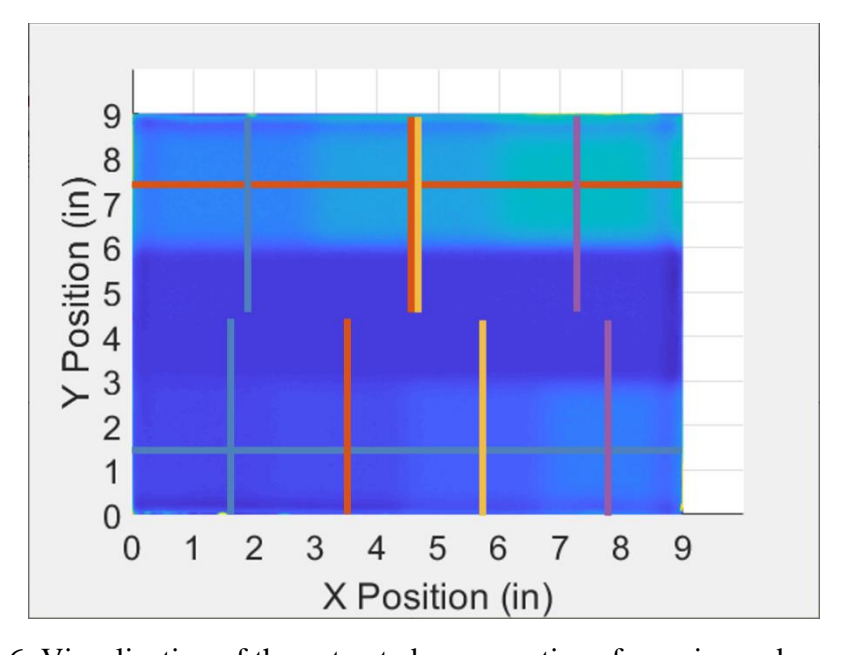


Figure 5-6: Visualization of the extracted cross sections for series and parallel data.

From the isolated transition zones, the dataset roughly looked like complementary error functions. Curve fits defined by Equation 5.1 were applied to each individual isolated transition zone. From the curve fit error functions, the derivative was taken to obtain a Gaussian pulse, then finally the mean plus three standard deviations was used to create the upper boundary and the mean minus three standard deviations was used to create the lower boundary. With the two boundaries defined, a transition zone width could be determine from the difference of the boundaries. A sample curve fit with its defined boundaries is shown in Figure 5-7.

$$y = a * erfc(bx + c) + d$$
 5.1

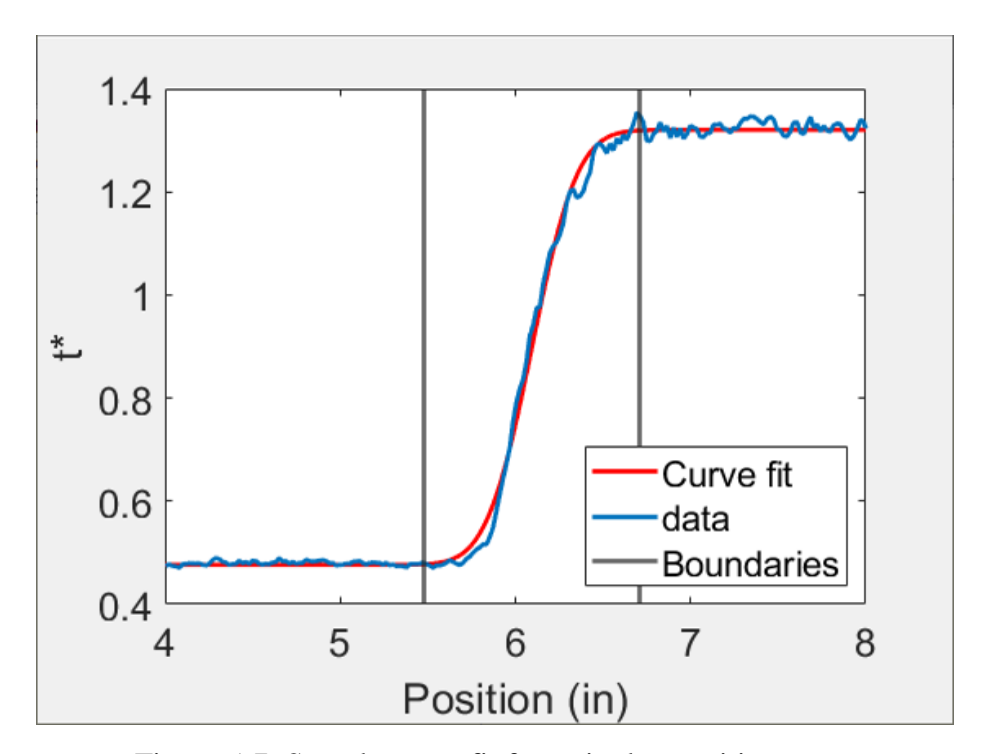


Figure 5-7: Sample curve fit for a single transition zone.

## 5.4 Results and Discussion

Transition zone widths were organized as ascending normalized steps (dL/L) and plotted as a bar chart in comparison with the respective prediction from Equation 3.2 with L and dL values

from the machined geometry section of Table 5-1. The bar chart comparisons are shown in Figure 5-8. The most notable thing about these results is that the prediction equation nearly matches the transition width obtained for the experiment for the five largest dL/L combinations tested while there is no clear trend for all other tested values.

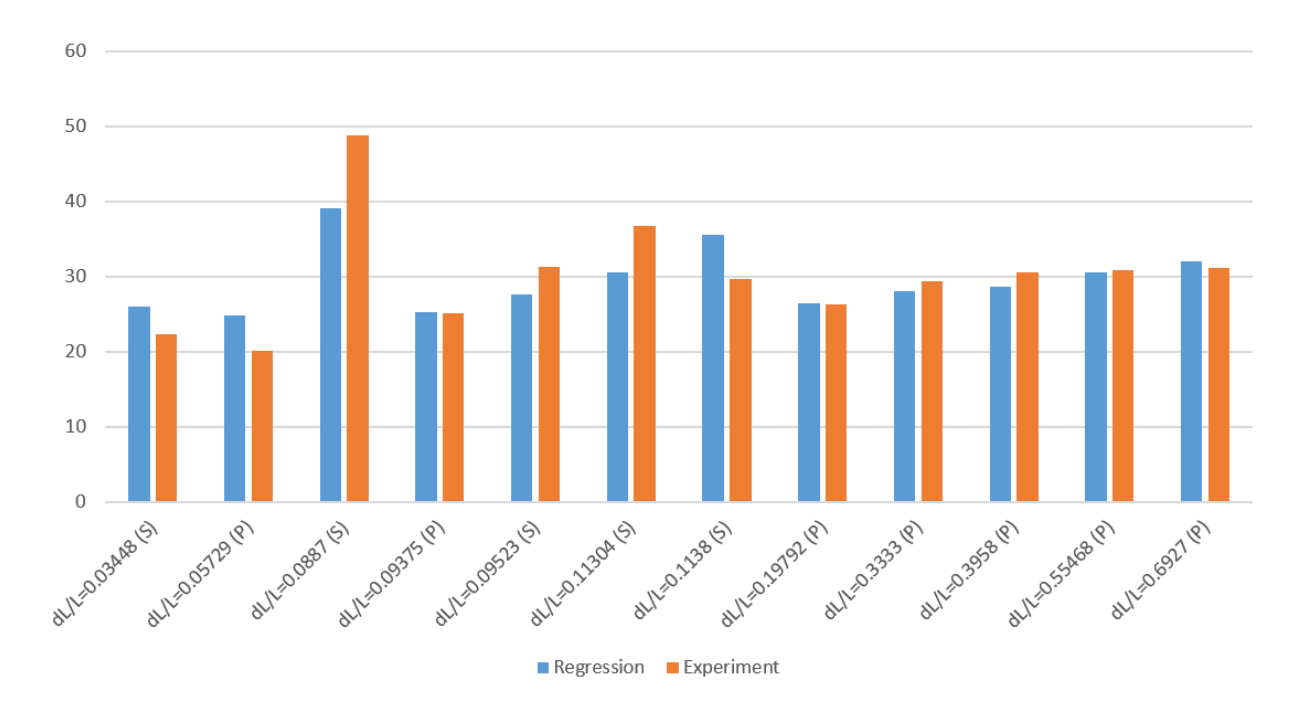


Figure 5-8: Transition zone comparison across series (S) and parallel (P) normalized steps.

Initially, these results seemed to indicate that there was a possible difference in behavior between the series and parallel steps. However, further modeling of series steps was performed and it was found that under ideal conditions where there is no overlap between transition zones (as the plate was designed), the behavior of the transition zone should be identical for either of the step structures. This further led into an investigation of the temperature difference across the step at time t\* to indicate if the transition zone could be properly assessed based on the temperature drop.

Data was acquired using a newly acquired temperature-calibrated commercial Flash Thermography system [17], including a camera operating at 120 Hz and xenon flashlamps. The data was processed using TSR once again and then temperature data was exported as a .dat file and input into MATLAB.

The data was again cropped and scaled so that only the plate was visible in the plotted area. Similarly, cross sections were taken based on the same schematic as was used to develop Figure 5-6 and these new temperature cross sections can be seen in Figure 5-9.

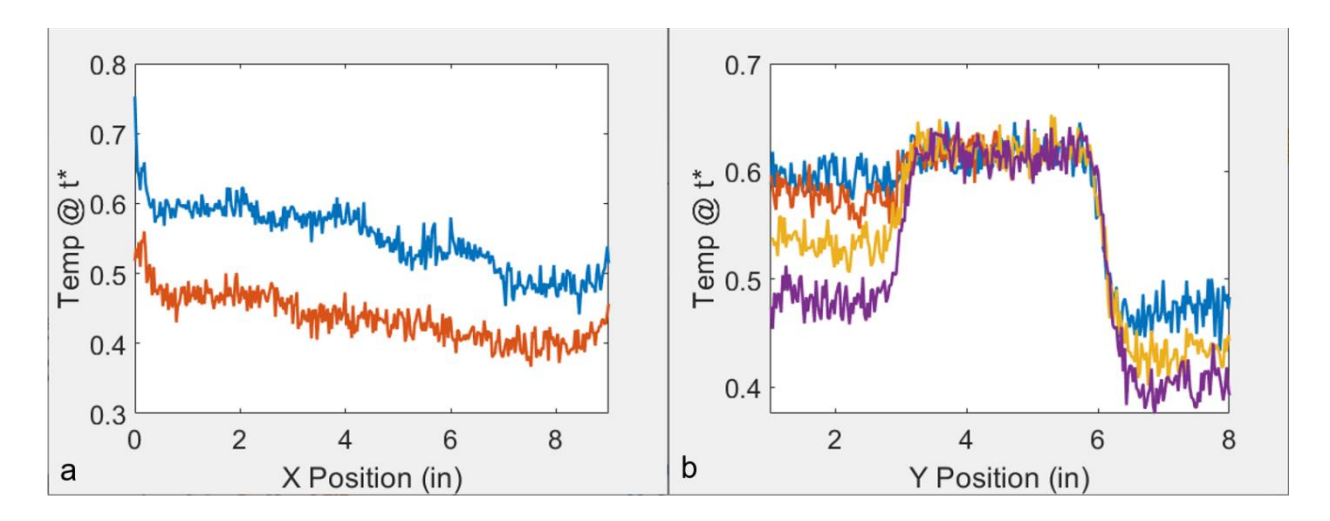


Figure 5-9: a) Series and b) parallel temperature data at time t\*.

Figure 5-9 highlights the problem that has caused the poor measurement of the transition zone width in the designed experiment. Due to noise levels in the temperature data, it becomes difficult to discern small steps from one another. With the temperatures so close to each other, it becomes difficult to differentiate the two, causing the transition zone measurements below a certain temperature threshold to be meaningless. Once again, complementary error functions were fit to individual sections, but now with the goal of finding the temperature drop across each section. With the temperature drop identified, it can be used together with the previously measured transition zone width to approximate a threshold for temperature drop which produces

a good transition zone measurement. While not all error functions fit well due to noise, an example of a good fit is shown below in Figure 5-10. The computed temperature drops from the experiment were then compared to the theoretical temperature drop using Equation 4.5, and a least square fit was implemented to determine the optimal heat flux of  $= 8600 \, J/m^2$ .

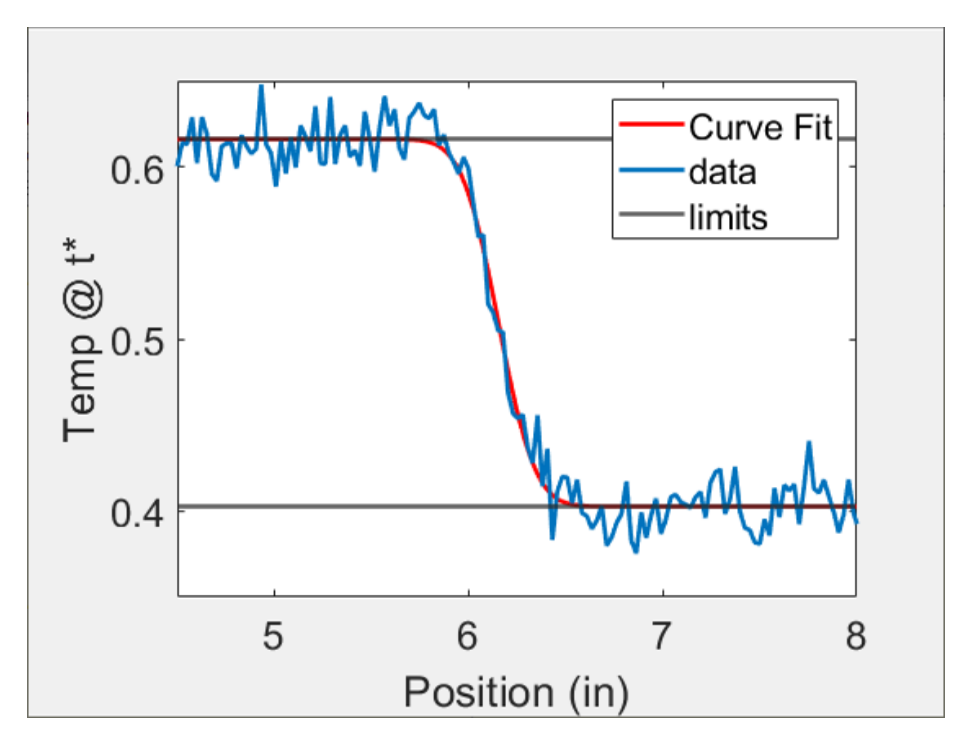


Figure 5-10: Sample temperature curve fit for a single step.

Figure 5-11 compares the accuracy of the experimentally measured temperature drop to its theoretical temperature drop. Below a certain threshold, while our temperature drops may be accurate when compared to the theoretical value, the ability to measure the transition zone accurately no longer exists. That limiting value was found to be about 90 mK.

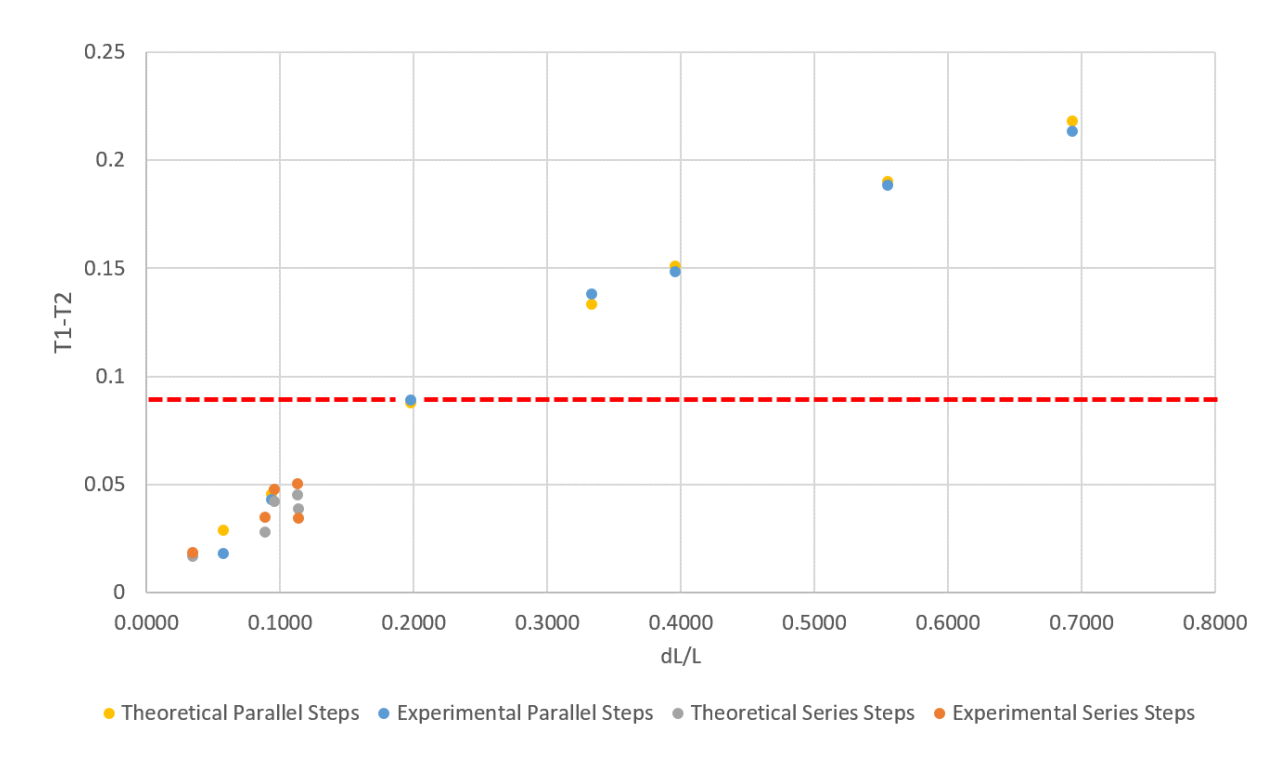


Figure 5-11: Temperature drop across all steps. A threshold for temperature drop in order to obtain a proper transition zone measurement was estimated to be at 90 mK.

# Chapter 6: Summary and Future Work

## 6.1 Summary

In this work, it was shown that the presence of a subsurface backwards facing step induces a measureable and predictable transition zone in the region near the step. By modeling the flash thermography process across three different materials with different diffusive time scales and across a range of geometries, it was shown that the transition zone can be defined simply as a function of its geometry. Experiments show that the model predictions work reasonably well under the assumption that the steps are properly distinguishable from each other. Additionally, an equation to estimate the detectability of a step was derived to be used in addition to the camera's detection limits. Utilization of the empirical transition zone equation in addition to the detectability equation should be sufficient to provide information on: a) if a subsurface step is detectable and significant, and b) the effects of the transition zone on the ability to obtain necessary IR NDT measurements within the part. Figure 6-1 highlights the transition zones that were properly measured and that when steps are properly distinguishable and there is a large enough temperature drop across a step, the predictions work quite well.

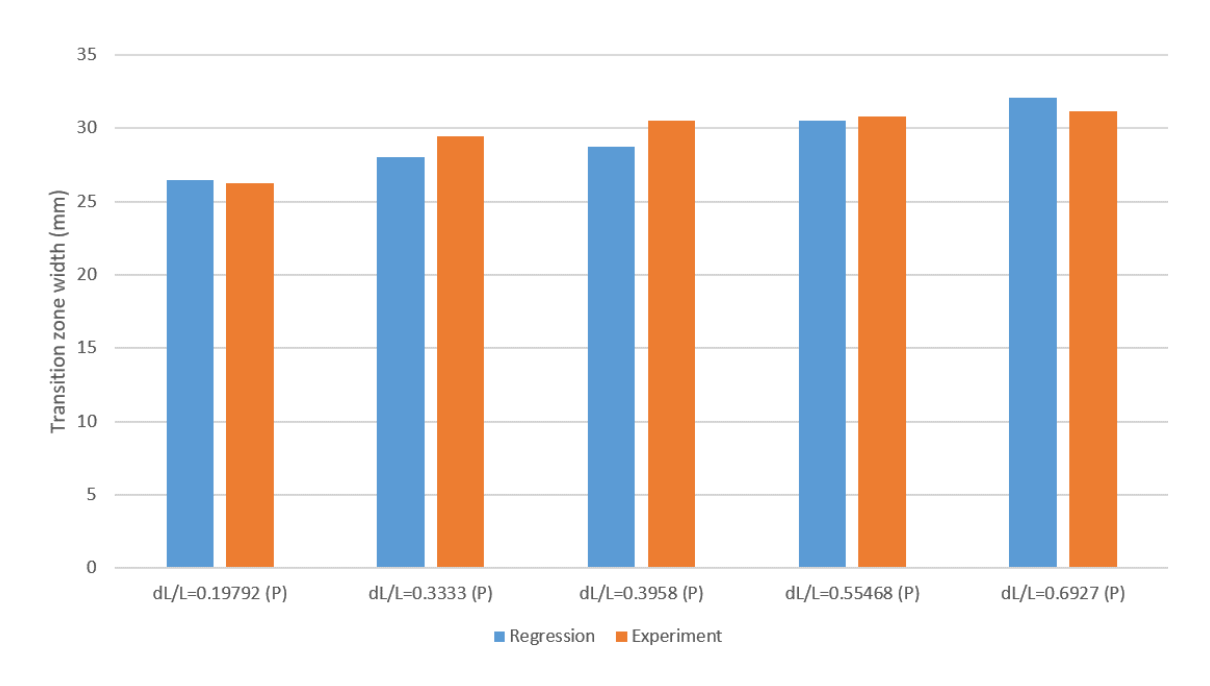


Figure 6-1: All properly measured transition zones.

## 6.2 Future Work

This future work for this project is split into three sections. Section 6.2.1 details short term recommendations which follows the experiments from Chapter 5. A sample was designed to extend the work in Chapter 5, but due to time constraints and machining problems, this experiment was not completed. Section 6.2.2 details how this work could be used as a basis to extend this work to new materials and geometries. Finally, Section 6.2.3 briefly details the possibility of using some sort of signal transformation to as an alternative route to data analysis.

#### 6.2.1 Immediate Extension of Work

From Figure 5-11, we defined a temperature drop threshold of 90 mK since it was at this point where we could last properly measure a transition zone., The sample can be modified such that previously poorly measured steps may benefit from such modification. To modify the sample, the flat section can simply be ground down while still maintaining the same step sizes that were previously created.

Careful consideration must be taken in order to choose how much to grind from the flat portion of the sample. If too much material is removed, then the capability to form a proper derivative vanishes as the heat will diffuse too fast through the thin sections. Once the ability to form a derivative is gone, we cannot confidently extract proper data to create a transition zone measurement. Grinding must also be done such that enough material is taken off to improve measurement of previously improperly measured steps. In order to decide how much to grind, the camera's characteristics and the steel material properties were used to determine the thinnest section possible in order to form a good derivative in TSR. Equation 6.1 was utilized to determine how thin a section can be to form a good derivative. This equation was formed by using the number of frames needed for good differentiation, n, and the camera's framerate, f, in combination with Equation 1.5.

$$L = \sqrt{\frac{n}{f}\pi\alpha}$$
 6.1

The number of frames was chosen to be 25 and the camera operates at 120 Hz. Using steel's properties from Table 2-1, the minimum thickness was estimated to be 3.0 mm. This corresponds to removing 1.8 mm from the flat side of the plate. With this information, a new prediction for temperature drop can be generated as Figure 6-2. Using the defined cutoff as 90 mK, the new sample should allow for an additional 8 points (6 parallel and 2 series) at minimum to be added to the dataset of good measurements. Combined with the previous 5 accurate measurements of the transition zone, 13 total measurements should be available to compare to the predictive equation for transition zone width.

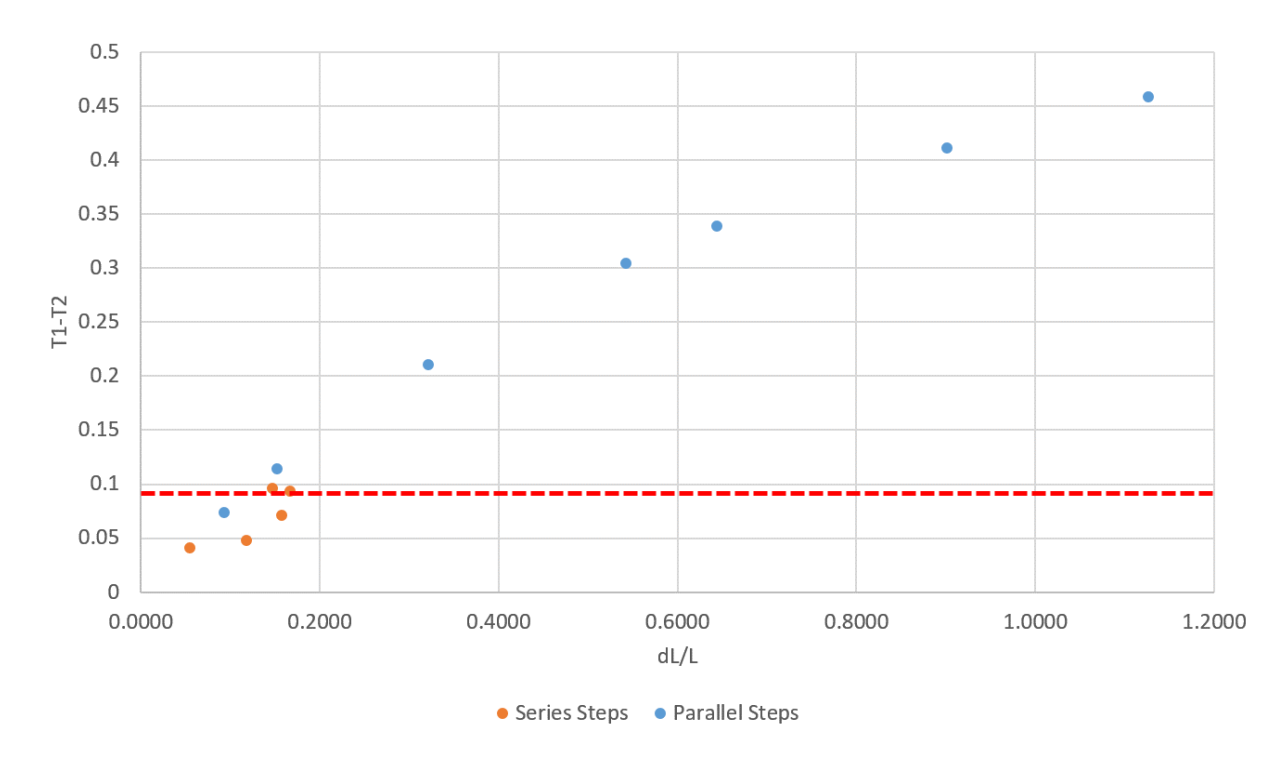


Figure 6-2: Prediction of temperature drop across modified sample utilizing the same temperature threshold of 90 mK.

When attempting to grind the plate for this experiment, there were mounting problems with grinding the sample as the side with the uneven steps was being held on the machine leading to leveling issues. Further some sections were too thin and there was a risk of breaking the plate. Hence, instead of machining the old sample, a new plate needs to be machined to have the same dimensions of the ground plate.

## 6.2.2 Extension to Composites and Joints

While the bulk of this work was done on steel to simplify the problem at hand to an isotropic material, the main application still lies in composite materials. In this work, we simplified the composite and assumed it to be a material with isotropic heat conduction. In reality, this is not the case and oftentimes the conduction along the fibers can be up to 10x higher than the through thickness conduction [18], resulting in an order of magnitude faster diffusion along the fibers.

This increased in diffusivity will undoubtedly lead to an alteration of the transition zone. While anisotropy was briefly looked at during this project, not enough work was done on it to make any sound conclusions that would have a substantial impact on this thesis. If we aim to truly and accurately describe the subsurface geometry effects on flash thermography in composites, work relating to varying the ratio of the through-thickness and in-plane diffusivity would need to be done in order to obtain some sort of general expression for the transition zone width for anisotropic diffusion.

Additionally, instead of looking at geometrical effects on the diffusion, we also need to study how defects affect signals from flash thermography in composite materials. This would be done, for example, by modeling a composite joint with adhesive layers and including defects above or below the bondline. Here, each material discontinuity (composite / adhesive / defect) would have an effect on the signals in flash thermography. Modeling this behavior would help to provide more clarity into experiments as the models can help inform us as to how the material discontinuity affects the derivatives of the temperature data, which in turn would allow us to properly discriminate real defects and material interfaces in an experimental setup. For simplicity, it makes sense to begin with another isotropic assumption, but addressing anisotropy could provide some additional accuracy to the problem.

## 6.2.3 Alternative Data Processing Methods

In this analysis, when determining and investigating the finite width of the transition zone, a two pulse Gaussian function fit was employed. This was done as it would easily allow us to use the well-known properties of the Gaussian functions in order to define boundaries to the transition zone. However, another method may prove to be more robust and provide a more physical meaning to the problem at hand. Fourier Transforms are often used in Engineering

Signal processing and could be a future avenue to explore for data analysis of the signals resulting from the transition zone data. Nevertheless, other signal transform methods may prove to be a more useful analysis methods but would need to be fully explored to characterize their capabilities at analyzing the problem.

**APPENDIX** 

#### **APPENDIX**

```
% InitPoints is the starting window size. for 3 point derivative set
Initpoints to 3
% GrowStart is the percentage in the x axis where you want to window stat to
% Grow. suggested value is 0.75 to start grow window size at three quarters
% the data range. this parameter controls how much smoothing is applied to
% derivative calculation
function der = NumericDerivative( x, y, InitPoints, GrowStart)
   Radius = (InitPoints-1)/2;
    len = length(x);
    th = x(1) + (x(end) - x(1))*GrowStart;
    der = zeros(len, 1);
    for i = 1:len
        if(x(i) < th)
            startindex = max(1, i-Radius);
            endindex = i + Radius;
            if(endindex > len)
                endindex = len;
                startindex = endindex - InitPoints;
            end
            MaxInterval = x(endindex) - x(startindex);
        else
            R = Radius;
            interval = x(min(len,i+R)) - x(max(1,i-R));
            while(interval < MaxInterval && i - R > 1)
                R = R + 1;
                startindex = max(1, i-R);
                endindex = i+R;
                % window has reached end of range. shift left boundary to
                % maintain window size
                if(endindex > len)
                    endindex = len;
                    while(x(startindex) > x(endindex) - MaxInterval)
                            startindex = startindex - 1;
                    end
```

```
break;
                end
                interval = x(endindex) - x(startindex);
            end
        end
        der(i) = CalSlope(x,y,startindex,endindex);
    end
end
% linear fit slope calculation
function S = CalSlope(x,y,startindex,endindex)
    SumX = 0;
    SumY = 0;
    SumXY = 0;
    SumXSquare = 0;
    count = 0;
    for m = startindex:endindex
        SumX = SumX + x(m);
        SumY = SumY + y(m);
        SumXY = SumXY + x(m) * y(m);
        SumXSquare = SumXSquare + x(m) * x(m);
        count = count + 1;
    end
    SSxy = SumXY - (SumX * SumY)/count;
    SSxx = SumXSquare - (SumX * SumX)/count;
    S = SSxy/SSxx;
end
```

**WORKS CITED** 

### **WORKS CITED**

- [1] Ciampa, F., Mahmoodi, P., Pinto, F., & Meo, M. (2018). Recent advances in active infrared thermography for non-destructive testing of aerospace components. Sensors (Switzerland), 18(2). https://doi.org/10.3390/s18020609.
- [2] Siegel, J. E., Beemer, M. F., & Shepard, S. M. (2020). Automated non-destructive inspection of Fused Filament Fabrication components using Thermographic Signal Reconstruction. Additive Manufacturing, 31(October 2019), 100923. https://doi.org/10.1016/j.addma.2019.100923.
- [3] Sfarra, S., Theodorakeas, P., Ibarra-Castanedo, C., Avdelidis, N. P., Paoletti, A., Paoletti, D., Hrissagis, K., Bendada, A., Koui, M., & Maldague, X. (2011). Importance of integrated results of different non-destructive techniques in order to evaluate defects in panel paintings: the contribution of infrared, optical and ultrasonic techniques. O3A: Optics for Arts, Architecture, and Archaeology III, 8084(June 2011), 80840R. https://doi.org/10.1117/12.889335.
- [4] Cheng, L., & Tian, G. Y. (2012). Comparison of nondestructive testing methods on detection of delaminations in composites. Journal of Sensors, 2012. https://doi.org/10.1155/2012/408437.
- [5] Ducar, R. J. (1999). Pulsed thermographic inspection and application in commercial aircraft repair. Thermosense XXI, 3700(March 1999), 77–83. https://doi.org/10.1117/12.342277.
- [6] Baughman, S. R. (1998). Applications for thermal NDT on advanced composites in aerospace structures Thermosense XX, 3361(March 1998), 311–319. https://doi.org/10.1117/12.304742.
- [7] Shepard, S. M. (2007). Automated processing of thermographic derivatives for quality assurance. Optical Engineering, 46(5), 051008. https://doi.org/10.1117/1.2741274.
- [8] Theodorakeas, P., Avdelidis, N. P., Hrissagis, K., Ibarra-Castanedo, C., Koui, M., & Maldague, X. (2011). Automated transient thermography for the inspection of CFRP structures: experimental results and developed procedures. Thermosense: Thermal Infrared Applications XXXIII, 8013(May 2011), 80130W. https://doi.org/10.1117/12.882695.
- [9] Carslaw, H. S., & Jaeger, J. C. (2011). Conduction of heat in solids. Clarendon Pr.
- [10] Krapez J.C., Balageas D., Deom A., Lepoutre F. (1994) Early Detection By Stimulated Infrared Thermography. Comparison With Ultrasonics and Holo/Shearography. In: Maldague X.P.V. (eds) Advances in Signal Processing for Nondestructive Evaluation of Materials.

- NATO ASI Series (Series E: Applied Sciences), vol 262. Springer, Dordrecht. https://doi.org/10.1007/978-94-011-1056-3\_23.
- [11] Maldague, X. P. V. (1993). Nondestructive evaluation of materials by infrared thermography. Springer.
- [12] Shepard, S. M. (2007). Flash Thermography of Aerospace Composites. 1–7. http://www.ndt.net/article/panndt2007/papers/132.pdf.
- [13] Omar, M. A., & Zhou, Y. (2008). A quantitative review of three flash thermography processing routines. Infrared Physics and Technology, 51(4), 300–306. https://doi.org/10.1016/j.infrared.2007.09.006.
- [14] Balageas, D., Chapuis, B., Deban, G., & Passilly, F. (2010). Improvement of the detection of defects by pulse thermography thanks to the TSR approach in the case of a smart composite repair patch. Quantitative InfraRed Thermography Journal, 7(2), 167–187. https://doi.org/10.3166/qirt.7.167-187.
- [15] Shepard, S. M., Lhota, J. R., & Ahmed, T. (2007). Flash thermography contrast model based on IR camera noise characteristics. Nondestructive Testing and Evaluation, 22(2–3), 113–126. https://doi.org/10.1080/10589750701448662.
- [16] FLIR Systems, Inc, (2019). FLIR A6751, 29440-251.
- [17] EchoTherm, Thermal Wave Imaging, Inc, Madison Heights, MI.
- [18] Tian, T., & Cole, K. D. (2012). Anisotropic thermal conductivity measurement of carbon-fiber/epoxy composite materials. International Journal of Heat and Mass Transfer, 55(23–24), 6530–6537. https://doi.org/10.1016/j.ijheatmasstransfer.2012.06.059.